Eötvös Loránd University
Faculty of Natural Sciences
Institute of Physics

Numerical and experimental study of superconducting magnetic shields for the construction of a high field septum magnet

Novák Martin István
Physicist MSc

Supervisor:
Barna Dániel
MTA Wigner Research Centre for Physics

Consultant:
Horváth Ákos
ELTE TTK Department of Atomic Physics

31th May 2018

Abstract

Since its formation, particle physics is a focus point both in theoretical and in experimental physics. Beautiful and elegant theories were developed by theorists and then justified by experimentalists. This was made possible by the technological innovations of the previous and the current decades. The Large Hadron Collider (LHC), the result of one of the biggest international scientific and industrial collaboration of humanity operates at higher energies than anything else, and it has made possible to discover the Higgs-boson.

Although the LHC will be upgraded to increase its luminosity by a factor of 10 (high-luminosity LHC, HL-LHC), and it is scheduled to run until around 2035, many open questions of particle and astrophysics will probably require even higher energies. To name a few: what is dark matter? What is the origin of the observed difference between the amounts of matter and antimatter in the universe? Is there supersymmetry?

Since the time-scale of the realization of accelerators of this large scale is about 20-30 years, the Future Circular Collider (FCC) Study was launched in 2014 in order to establish the conceptual design of a post-LHC proton-proton collider ring with 50+50 TeV collision energy, thereby ensuring the continuity of experimental high-energy particle and accelerator physics in Europe and in the world. The study must identify the key challenges and the required technological innovations, propose solutions and conduct a vigorous R&D programme to work out functional prototypes.

A key difficulty is the manipulation of the beam which has unprecedented rigidity. The beam will be kept in orbit by 16 T Nb_3Sn magnets. Another challenge is the enormous energy (8.4 GJ) stored in a single beam, which has to be safely disposed of the end of a collision cycle, or in cases of an emergency situation, without damaging the beam dump. The beam extraction system is affected by both issues. The septum magnets need to create very high magnetic fields($\geq 3T$) in the proximity of the circulating beam, where the magnetic field needs to be zero. A high field is required to make the magnet system compact and leave space for protection elements against the destructive effect of even a single bunch in case of a failure scenario.

In this work, I am investigating the feasibility of using a passive superconducting magnetic shield inside a superconducting magnet to realize the field configuration of the septum magnet. In particular, I report the test results of different superconducting shield materials and compare them to detailed finite-element simulations. These results indicate that this novel concept can be realized with practical superconductors. The thesis also presents a preliminary design of the device.

Contents

1. Introduction

This section summarizes the history of particle accelerators based on an existing, really detailed work [1], their working principle and a short overview of their current state and their possible future improvements. Furthermore, I will shortly summarize the theoretical basis of superconductors and the Finite Element Method which I'm using in my numerical simulations.

1.1. Particle accelerators

1.1.1. History

The history of particle accelerators goes back to the beginning of the 20th century when scientists started to develop theories of the atomic structure. In 1911 Ernest Rutherford disproved J.J. Thompson's famous "plum pudding" model of atoms. He used α-particles emitted by a radioactive element to "scan" the inner structure of the atom. Other experiments suggested that atoms have an even more complex structure. To discover this structure, the energy of α-particles from radioactive decay was not enough. Rutherford visioned particle accelerators of a few MeV kinetic energy as viable tools for further experiments. The first artificial particle accelerator was constructed by John Cockroft and Ernest Walton based on a simple voltage multiplier, which could accelerate the particles to 800 keV energy. In 1932 they have successfully split the lithium atom [2] and earned a Nobel Prize with their discovery in 1951. At that time the other alternative was the famous Van de Graaff generator which could reach 1.5 MV potential at first, but with certain improvements like putting it in a high-pressure tank and making it a tandem accelerator, similar devices can reach energies up to 15 MeV.

The problem with electrostatic accelerators is that it is difficult to maintain the high voltage in a small space, because of spark formation. To solve this problem, Gustav Ising developed the concept of the pulsed drift tubes. The basic difference between the Ising's suggestion and the Cockcroft-Walton accelerator is that in Ising's idea the electric field is not static. Since the electrostatic field is conservative, accelerators using a static field in a circular geometry won't have any net accelerating effect. Rolf Widerøe developed the concept further and constructed the first linear accelerator, where drift tubes were connected to an RF*(Radio Frequency)* generator which determined the frequency of the accelerating field. Since the applied frequency was constant, to ensure that the particles are feeling the field in the right direction, each drift tube has to be longer than the previous one. This is the basic principle of the modern linear accelerators which are really important in many fields of life in spite of their simplicity.

From Widerøe's work, Ernest Lawrence noticed that a similar acceleration effect can be achieved with a circular geometry. Lawrence used Widerøe's idea that the particles should be accelerated in discrete steps. In Lawrence's cyclotron, the particles are accelerated in the gap between two hollow half-cylindrical electrodes (the so-called "dee" electrodes, named after their

shape), which are connected to an RF generator. The particles are bent back to the same gap by a magnetic field on a semi-circle with a radius of.

$$r = \frac{p}{qB} = \frac{mv}{qB} \tag{1.1.1}$$

As long as the particles are non-relativistic, $p = mv$ and this guarantees a momentum-independent revolution frequency (the cyclotron frequency), so that the particles remain in synchrony with the RF field. When the particles become relativistic, the radius of their trajectory keeps increasing but their velocity saturates, which breaks down synchronism with the RF field.

The relativistic limit problem can be solved by the synchro-cyclotron, where the frequency of the electric field is decreased during operation as the energy of the particle increases, or by the azimuthally varying field (AVF) cyclotron. The other limitation of the cyclotron is the size of the device. Because the radius of the particle orbits is increasing with the energy of the particle, higher energies would require bigger cyclotrons, which obviously limits their usage. This problem can be solved by keeping the orbit radius constant with an increasing magnetic field.

The Betatron tried to solve the size problem of the cyclotron. Using Faraday's law

$$\oint_{\partial S} \mathbf{E}\,\mathrm{d}\mathbf{r} = -\frac{\mathrm{d}}{\mathrm{d}t}\int_S \mathbf{B}\,\mathrm{d}^2\mathbf{r} \tag{1.1.2}$$

we can see that the change of the magnetic flux enclosed by the nominal particle orbit induces electric field along the beam axis. This flux is caused by the current change in the primary coil.

From Ampere's law the

$$B\left(r\right) = \frac{1}{2}\left\langle B\right\rangle \tag{1.1.3}$$

where $B\left(r\right)$ is the magnetic field at radius r (the nominal orbit), and $\langle B\rangle$ is the average field within the orbit. Betatron-principle can be easily derived [1]. This formula means that the average magnetic field which is responsible for the acceleration is the half of the guiding magnetic field. In this device, both the guidance and the acceleration of the beam come from the same field. The magnetic field is increased with time, to keep the particles on nearly constant orbits, and to induce the accelerating electric field. The highest achievable energy is limited by the saturation of the iron. The largest achieved energy for electrons with betatron is 300 MeV.

If the accelerating electric field is generated by an independent RF system and not by the same magnetic field, which keeps the particles on the circular orbit, it is sufficient to produce a magnetic field only at the location of the circulating orbit, and increase it proportionally to the momentum of the particles to keep the orbit constant. This makes the magnet system much simpler and smaller, and allows to increase the accelerator's radius - and thereby its maximum energy - very significantly. Since the particle orbit is constant, the frequency of the accelerating field needs to be changed too during acceleration, as long as the particle velocity is increasing with increasing momentum. Besides these, the other principle which makes the operation of the synchrotrons possible is phase stability which was discovered by Veksler in 1945. This design

solves the size and the relativistic limitations of the cyclotrons, and has many other advantages, for example, one can use two beams circulating in the opposite direction, and this way the centre of mass energy is significantly larger than in the fixed-target case.

1.1.2. Benefits of Accelerators

Particle accelerators have a broad range of applications not only in science but also in civil life starting from medicine through semiconductor industry to cleaning water and air.

In medicine linear accelerators are widely used in radiation therapy to treat people with tumours near the 'surface' of the body or to produce different radioactive isotopes of materials, like producing radioactive cobalt for a so-called 'cobalt-gun' which is used to treat tumours lying deep inside the body. They are also important in medical imaging, like X-ray, CT and PET, or in the sterilisation of medical tools. For this purpose usually, electron beams are used.

In biophysical research and in the pharmaceutical industry the strong X-ray beams provided by synchrotron light sources can be used in X-ray crystallography to quickly determine the 3D structure of proteins with an important role in the human body. This is often really helpful to understand its function and 'way of working' in the human body, which can help to understand sicknesses caused by the absence or inappropriate working of the molecule. Also, most of the receptors in the brain are also proteins, so if the receptor structure is determined, one can design drug molecules that bind with high affinity to a specific receptor. These synthetic drug molecules are often mimicking other molecules that can be naturally found in the human body.

Accelerators are also used in the semiconductor industry for ion implantation. This basically enables the fine-tuning of the switching threshold of MOSFETs, like CMOS transistor which is essential in almost every modern portable electronic device due to its low energy consumption.

Accelerators find application in food industry as well. Heat shrinking foils used in the packaging process are usually made from polyethene, which is a polymer, where each carbon atom bonds to another two carbon and two hydrogen atoms. After this, the material is irradiated with electron beam, which knocks out a hydrogen atom.

Figure 1.1: Radura symbol

The 'freed' valance electron forms a bond with another carbon atom, which is much more stronger than the previous carbon-hydrogen bond. The result of this process is a stronger material which won't melt if it is heated up to its boiling temperature but shrinks instead. Furthermore, if a food has the symbol shown in Fig. 1.1, on its package, that means that it has been irradiated to clean it and improve shelf time.

1.1.3. The LHC

The Large Hadron Collider*(LHC)* s the topmost accelerator ring in CERN's accelerator hierarchy (Fig. 1.2), which is located in an accelerator complex under of the border of Switzerland and France. Currently the LHC is the largest in the world with the highest beam energy.

In the LHC the protons are provided by a duoplasmatron source which ionizes hydrogen gas using an electron beam. The electrons are removed from the hydrogen particles with an electric field, resulting in protons, which are accelerated by LINAC 2 to 50 MeV. The beam is then injected into the Proton Synchrotron Booster *(PSB)*, which is the injector accelerator of the Proton Synchrotron*(PS)* and accelerates the protons to 1.4 GeV. They reach 25 GeV energy in the PS and then they are injected into the Super Proton Synchrotron*(SPS)*, which accelerates them to 450 GeV. The SPS is the last step of the acceleration of the protons before the LHC, where they reach 6.5 TeV energy in 20 minutes after the injection [3].

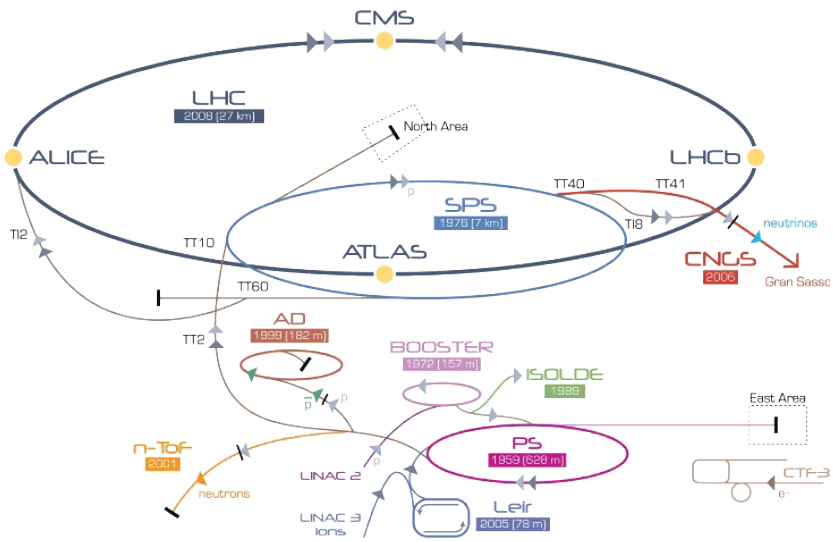

Figure 1.2: Schematic layout of the accelerators of CERN

There are four large experiments placed in the LHC ring. The CMS*(Compact Muon Solenoid)* searches for new physics like dark matter or gravitons. The ATLAS*(A Toroidal LHC ApparatuS)* has the same goal as the CMS, but it uses different technology. [4]. In 2012 these two detectors independently discovered the famous Higgs-boson, the missing brick from the Standard Model. ALICE*(A Large Ion Collider Experiment)* is designed to study the quark-gluon plasma and help

us to understand what happened right after the Big Bang. The LHCb*(Large Hadron Collider beauty)* experiment measures the decay of hadrons containing a bottom quark which could explain the matter-antimatter imbalance.

Physics start date	2009	2015	2023
Particles collided	*pp*		
Maximum beam energy [TeV]	4.0	6.5	7.0
Luminosity $\left[10^{30}\frac{1}{cm^2 s}\right]$	$7 \cdot 10^3$	$2 \cdot 10^4$	$5 \cdot 10^4$
RF Frequency [TeV]	400.8	400.8	400.8
Particles per bunch $\left[10^{10}\right]$	16	12	22
Bunch per ring	1380	2508	2760
Circumference [km]	26.659		
Dipole magnet length [m]	14.3		
Standard cell length [m]	106.9		
Dipoles in ring	1232		
Quadrupoles in ring	506		
Peak magnetic field [T]	8.3		

Table 1: A few parameters of the LHC

From the viewpoint of this work, the most important parameters of the LHC are summarised in Table 1. The beam is kept on orbit by superconducting dipole magnets and focused by quadrupole magnets. There are two special magnets involved in the beam injection and extraction process, the kicker magnet, and the septum magnet.

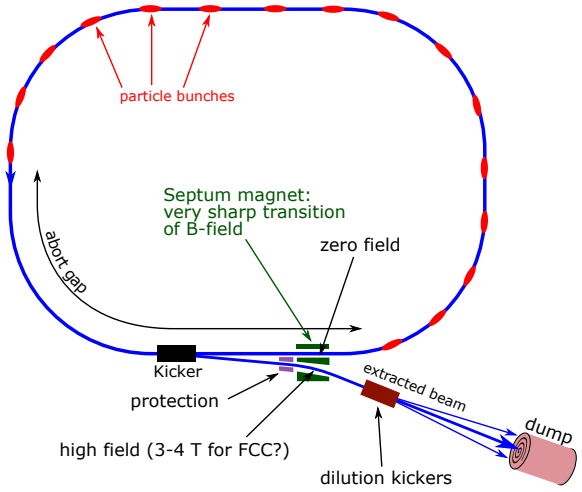

Figure 1.3: Beam extraction scheme

Figure 1.3 shows the schematic representation of the beam extraction in the LHC. The same extraction scheme is planned for the Future Circular Collider as well. In the injection process a particle-free abort gap is created along the ring circumference. When the beam is extracted, the kicker magnet is very quickly (≈1 μs) switched on, synchronized with the passage of the abort gap through the magnet, and reaches full field before the first bunch after the abort gap arrives. The beam receives a small kick and starts to diverge from the nominal orbit. Then it runs into a stronger magnet, called the septum magnet, which creates zero field at the position of the circulating orbit, and a high field at the position of the extracted beam, very close to the circulating beam. The extracted beam is then swept by a "dilution kicker" magnet system in order to distribute the beam energy over the entrance face of the beam dump. The systems used in beam extraction and injection have to be extremely reliable since even one fail of the kicker or the septum magnets could heavily damage the accelerator.

The LHCs beam dump system uses 15 kicker magnets*(MKD)* [6]. The kicker is a magnet which could reach its nominal field just in a μs. To reach this fast rise-time, very low (<250 nH) [6] inductance transmission lines required between the magnets and their pulse generators. Also, magnet inductance needs to be low and therefore these magnet use single-turn coils. The pulse generators are based on capacitors and thyratron switches. The circuit is duplicated due to reliability reasons. If a unit accidentally misfires, all other units are triggered within 1 μs.

The LHC has 15 so-called Lambertson-septum magnets*(MSD)* of three different types. These magnets operate in quasi-DC mode, meaning that their magnetic field follows the actual beam momentum in the ring, being ready for an emergency beam abort at any time. This is necessary because such a high field cannot be switched on as quickly as it should be in case of a failure scenario. Septum magnets are typically realized either having a physical current-carrying wall, or a ferromagnetic material between the two regions with high and zero magnetic fields, in order to create the sharp jump over a small distance (*septum* in Latin means a wall separating two cavities). This wall is called the *blade*.

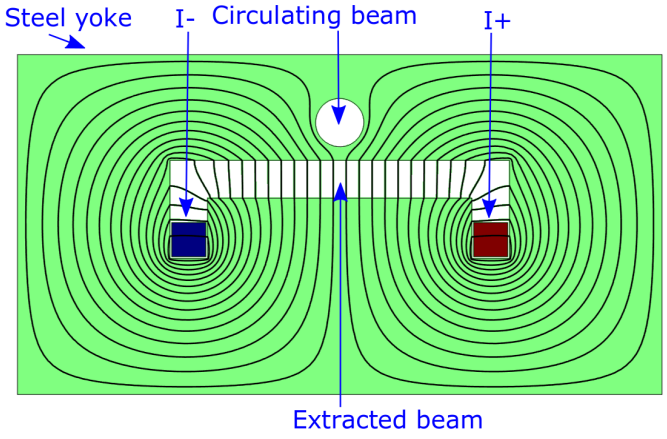

Figure 1.4: A schematic figure of the Lambertson septum's cross section

The schematic representation of the Lambertson septum with the magnetic field induction lines is shown in Fig. 1.4. It is a very reliable device since it uses only conventional technologies. The septum has a steel yoke laminated from 1 mm thick steel plates with 10 μm Fe_3O_4 as insulator [6]. The homogeneous magnetic field is generated in the gap within the yoke. The circulating beam is protected from the septum's high field by the yoke itself due to its large permeability.

The horizontal and vertical dilution kicker magnets sweep the beam in a time-dependent way, synchronized such that the beam paints an 'e'-shape on the absorber. The dump is made from two different types of graphite cylinders. The dump core is surrounded by concrete blocks for radiation shielding. Protector elements TCDS and TCDQ are placed upstream of the extraction septa and a quadrupole magnet, respectively, in order to protect them from the beam in case of an asynchronous dump, when the beam is swept by the rising magnetic field of the kicker magnets into their mass. [6].

1.1.4. The FCC Project

Even though the LHC is the biggest accelerator in the world, and made groundbreaking discoveries, like the Higgs-boson, many questions are still unanswered about our Universe. It seems that the current energy of the LHC might not be enough to discover essentially new phenomena in the world, like superpartners of our current elementary particles, or the origin of the neutrino mass. The Future Circular Collider Project has been launched in 2014 and aims to design a particle accelerator in the high-energy frontier. The Conceptual Design Report (CDR) should be finished by the end of 2018. The basic parameters of the FCC are shown in Table 2, compared to those of the LHC.

	FCC-hh	LHC
Beam energy [TeV]	50	7
Dipole field [T]	16	8.33
Circumference [km]	97.75	26.7
Bunch intensity $\left[10^{11}\right]$	1	1.15
Bunch spacing [ns]	25	25
Synchr. rad. power [kW]	2400	3.6
Peak luminosity $\left[10^{34}\frac{1}{cm^2 s}\right]$	5	1
Events per bunch crossing	170	27
Stored energy per beam [GJ]	8.4	0.36

Table 2: Planned parameters of the FCC compared to the current parameters of the LHC

From Table 2 its easy to see the biggest challenges in the construction of the FCC. Because

the beam energy is more than 7 times higher, stronger magnets are needed to keep the radius of the particle orbit within acceptable limits. The superconducting cables used in the LHC magnets are made from NbTi filaments (6500) embedded into a 0.8 mm thick copper strand. A flat-cable is made from 36 of these strands. The biggest magnetic field that dipole magnets can produce with NbTi coils is around 10 T, because the upper critical field of NbTi is 14 T [8]. The FCC magnets will therefore use Nb_3Sn, which has upper critical field around 30 T, but other effects limit its practical usage to 17-18 T [8]. The construction of the 16 T accelerator magnets is a great challenge. Nb_3Sn is brittle, and the coils are therefore made using the "wind and react" technology: the coils are formed using a Nb-Sn mixture, and then heat treated above 650 °C to produce Nb_3Sn. Three different magnet configurations are considered, one is the regular $\cos\theta$ configuration where the coils are placed on a circular shape, and the current density along the coils is $J_z \propto \cos(n\theta)$ functions to create a $2n$-pole field. The other two is the "block coil" and the "common coil" solution.

The stored 8.4 GJ energy is more than 23 times bigger than the LHCs. The beam would penetrate through 300 m of copper if impinging on a single point, or melt 12 tonnes of copper. This enormous energy poses big challenges for the beam dump system design. The septum and the kicker magnets have to be extremely reliable, because even one failure could have terrible consequences. Even though the beam extraction could be solved with the LHC's Lambertson septa, and it would be beneficial because its a well-known, regular technology, septum magnets with higher field are highly desirable, to reduce the size of the system from 170 meters to 70 meters. There are two proposed solution, one is the SuShi*(Superconducting Sheild)* Septum, which will be described later in this work, the other is the so-called "Truncated Cosine-Theta" which is a modified version of the regular cosine-theta magnet.

While the beam in the LHC dump system only paints a simple 'e' shape on the beam dump, the dump pattern of the FCC is much more complex, due to the larger circumference (bunch train length) of the ring, and the higher particle energy. The baseline concept is a long spiral, which is realized by two (horizontal and vertical) dilution kicker systems, driven by sinusoidal waveforms with a phase difference of 90°, and amplitude decreasing with time. The oscillation frequencies in the two planes must be very well matched. A 10 per mille difference would lead to a locally increased energy deposition density, and more than 800 °C temperature increase in the dump material. [9]. Similarly to the LHC, the dump block will be made of two different types of graphite.

From the Table 2. we can see that the power of the synchrotron radiation will be more than 600 times higher than in the LHC which is important in the design of radiation protection, and in the design of the detectors, which receive the highest doses (100-5000 MGy). The transistors produced with the current technology cannot withstand this high radiation [10].

1.2. Superconductivity

Superconductivity is a phenomenon when different materials could conduct electric current without resistance, and act like an ideal diamagnet. This effect is observable in a domain defined by critical quantities, like temperature, current and magnetic field. Microscopically this effect is caused by the interaction between the electrons and phonons. Qualitatively one can imagine a lattice vibration which pulls two electrons closer together, like an attractive force. This attractive force can form so-called Cooper-pairs between the two electrons. In second-quantized description the Cooper-pairs can be seen as the elementary bosonic excitations of the superconducting materials. At low temperatures a condensation of these bosons happens and this causes superconductivity.

Even though superconductors have zero resistance they cannot support arbitrarily large currents, because the magnetic field induced around the wire by the J_c critical current ruins this effect. Another interesting phenomenon is the Meissner-Ochsenfeld effect, which is the exclusion of the outer magnetic field from the material while it is cooled down. This effect can be understood by assuming that the outer magnetic field induces a thin surface current on the surface of the material which induces another magnetic field such that it cancels the external field on the surface, and shields the inside of the material. Because of the zero resistance, these currents will be persistent.

Superconductors can be divided into two categories, the type-I and the type-II superconductors. There are several differences between the two groups. In the case of type-I superconductors the Meissner-Ochsenfeld effect is only present in the case of weak external magnetic fields. The magnetic field is completely zero everywhere inside of the material until it reaches a critical $H_c(T)$ value which depends on the temperature. Above this field the material becomes completely normal conducting. This can be described with a first order phase-transition, so the critical magnetic field can be written in the form of:

$$H_c(T) = H_c(0)\left[1 - \left(\frac{T}{T_c}\right)^2\right] \tag{1.2.1}$$

Type-II superconductors have a lower critical field H_{c1} and an upper critical field H_{c2}. The magnetic field starts penetrate into the material continuously when H_{c1} is reached. The full penetration is reached at H_{c2}. The H_{c2} is usually orders of magnitude higher than the H_c value of type-I superconductors. For this reason, type-II materials are much more important in industrial applications than type-I. Below H_{c1} the material acts like a type-I one, above H_{c2} it acts like a normal conductor. Between the two critical temperatures there is the so-called Shubnikov-phase. In this phase superconducting and normal conducting domains are simultaneously present. The normal phase forms tube-like shapes, where the magnetic field can penetrate. The magnetic flux flowing through the tube is quantized. These tubes are also called vortexes, and form a regular grid. Every high-temperature superconductor is type-II.

1.2.1. Civil Life Benefits of Superconductors

The ongoing researches for the better understanding of superconductors, and solve room temperature superconductivity would solve many crucial problems of humanity. It could lead to a 4th industrial revolution, and it could have similar effects in the civil life, like the discovery of electricity. It could change almost every aspect of life, since it would revolutionize almost every industry.

The losses on power transmission lines can be as big as 15% between a power plant and an individual household. Using superconducting cables in the power-grids would result in a zero-loss electrical power transmission network. This could lead to a reduction in the price of electricity, but more importantly, a better utilization of the Earth's power sources in a more efficient way. The necessary cable thickness to transfer a certain current could also be significantly reduced.

Using superconducting cables is a double-edged sword, because the same idea could greatly reduce the power consumption of the electrical devices. There would be more energy available, but actually less would be needed. Revolutionary changes could be expected in the telecommunication industry too, because superconducting filter circuits could be much more precise than the ones with the current technology. This would result in the better exploitation of the current telecommunication bandwidth.

The diamagnetic properties of the superconductors could bring significant changes in the transportation systems. Instead of fossil fuel powered vehicles magnetic levitation could be used. The only resistance a vehicle would meet is the air drag. The superconducting motors and generators would also be a grondbreaking inventions. The lossless generators could be used in wind turbines, which would greatly improve their efficiency. The motors made from superconductors could bring the new era of road transportation by building very efficient electric cars. The introduction of superconductors in the transportation system could greatly reduce the fossil fuel dependence of humanity, and would be a great help to save the environment.

There are some scientific projects which results would have indirect effects in the civil life. The most famous one is the fusion reactor. Superconductors could carry enormous amount of current without heating up. This property makes possible to build very strong magnets to control the plasma in the reactors.

Medical devices also use superconductors, for example the Magnetic Resonance Image (MRI) is one of the most important non-invasive diagnostic device in modern medicine is based on very strong magnetic field. Even nowadays some machines are using superconductors, which of course have to be cooled which is very expensive. With room temperature superconductors this cost could be eliminated.

1.2.2. Electrodynamics of Superconductors

Some properties of the superconductors can be understood by assuming that Maxwell's equations remain unchanged, but the material equations have to be modified. Heinz London and his brother Fritz London assumed that next to the regular electrons new kind of "superelectrons" are present in the material with $-e^*$ charge, m^* mass, and n_s^* density. These new electrons do not participate in scattering processes. The current density they carry:

$$\mathbf{j}_s = -e^* n_s^* \mathbf{v}_s \tag{1.2.2}$$

Because of the assumption that the superelectrons do not scatter, they can accelerate freely in an electric field. From Newton's law:

$$m^* \frac{\mathrm{d}\mathbf{v}_s}{\mathrm{d}t} = -e^* \mathbf{E} \tag{1.2.3}$$

Substituting Eq. 1.2.2 into Eq.1.2.3 we get the first London-equation:

$$\frac{\mathrm{d}\mathbf{j}_s}{\mathrm{d}t} = \frac{n_s^* e^{*2}}{m^*} \mathbf{E} \tag{1.2.4}$$

Putting it back to Faraday's excitation law, and ordered to zero:

$$\frac{\mathrm{d}}{\mathrm{d}t}\left(\boldsymbol{\nabla} \times \mathbf{j}_s + \frac{n_s^* e^{*2}}{m^*} \mathbf{B}\right) = 0 \tag{1.2.5}$$

The London brothers assumed that the upper value not only constant in time, but the argument of the differentiation is zero in itself. Introducing the

$$\lambda_L^2 = \frac{m^*}{n_s^* e^{*2} \mu_0} = \frac{m_e}{n_s e^2 \mu_0} \tag{1.2.6}$$

quantity which is called the "London penetration depth", the London equations are:

$$\mathbf{E} = \mu_0 \lambda_L^2 \frac{\mathrm{d}\mathbf{j}_s}{\mathrm{d}t} \tag{1.2.7}$$

$$\mathbf{B} = -\mu_0 \lambda_L^2 \boldsymbol{\nabla} \times \mathbf{j}_s \tag{1.2.8}$$

In Eq. 1.2.6 we have assumed that $e^* = 2e$, $m^* = 2m_e$, $n_s^* = \frac{n_s}{2}$, because at the beginning of this section it has been stated that the superconductivity is caused by the Cooper-pair formation. This can be derived from the Bardeen–Cooper–Schrieffer (BCS) theory, but the microscopic description of superconductors is out of the scope of this work.

Taking the curl of Ampere's circuital law in the static case, the result is the second London equation:

$$\boldsymbol{\nabla} \times (\boldsymbol{\nabla} \times \mathbf{B}) = \mu_0 \boldsymbol{\nabla} \times \mathbf{j}_s = -\frac{1}{\lambda_L^2} \mathbf{B} \tag{1.2.9}$$

This equation can be easily solved if we take a half-infinite superconductor in the x direction and a homogeneous external magnetic field into the z direction. The solution is:

$$B_z(x) = \begin{cases} B_0, & x < 0 \\ B_0 e^{-\frac{x}{\lambda_L}}, & x > 0 \end{cases} \tag{1.2.10}$$

Substituting this back to Faraday's law, we get that the following current density is flowing on the surface of the material:

$$j_s = \frac{1}{\mu_0 \lambda_L} B_0 e^{-\frac{x}{\lambda_L}} \tag{1.2.11}$$

This current shields the inner magnetic field. The current density on the surface can not be larger than the current density which the critical magnetic field could induce:

$$j_c = \frac{1}{\mu_0 \lambda_L} B_c \tag{1.2.12}$$

1.2.3. Landau Theory of Superconductors

Despite its simplicity the London-model more or less can describe the most important properties of superconductors, another theories were developed for better accuracy. For example the Ginzburg-Landau theory of superconductors originally were developed to describe type-I superconductors without considering their microscopic properties, it predicted the existence of type-II superconductors. Landau and Ginzburg assumed, that the Landau theory of second order phase transitions can be applied to describe the normal-superconducting phase transition. In this theory there is a so-called order parameter which has finite value in the superconducting phase and zero in the normal phase and this transition is continuous. A free-energy can be defined as a functional of the order-parameter, and the minimum of this energy defines the equilibrium state. The free energy can be written as a series of the order parameter. Ginzburg and Landau assumed that the order parameter is related to the wave function of the electrons. Another assumption is that gradient of the order parameter present in the Taylor-series is related to the kinetic energy of the superconducting electrons electrons. The free-energy density is:

$$f_s = f_n + \alpha(T)|\psi|^2 + \frac{1}{2}\beta(T)|\psi|^4 + \frac{1}{2m^*}\left|\left(\frac{\hbar}{i}\nabla + e^*\mathbf{A}\right)\psi\right|^2 + \frac{1}{2\mu_0}(\boldsymbol{\nabla}\times\mathbf{A})^2 \tag{1.2.13}$$

In Eq. 1.2.13 the first term is the free energy of the normal conducting phase, α and β ar phenomenological parameters. The third term should be the gradient of the order parameter in the series, but it is replaced by the kinetic energy of the electrons. The last term is the energy stored in the magnetic field. To find the minimum the linear variation of the free-energy density as a functional of ψ and $\mathbf{A}$ has to be calculated:

$$\begin{aligned}\delta F_s = &\int_\Omega \mathrm{d}^3\mathbf{r}\left[\alpha\psi\delta\psi^* + \beta|\psi|^2\psi\delta\psi^* + \frac{1}{2m^*}\left(\frac{\hbar}{i}\nabla + e^*\mathbf{A}\right)^2\psi\delta\psi^* + c.c.\right] + \\ &+ \int_\Omega \mathrm{d}^3\mathbf{r}\left[\frac{\mathbf{B}}{2\mu_0}\boldsymbol{\nabla}\times\delta\mathbf{A} + \frac{e^*}{2m^*}\psi^*\delta\mathbf{A}\left(\frac{\hbar}{i}\nabla + e^*\mathbf{A}\right)\psi + c.c.\right]\end{aligned} \tag{1.2.14}$$

After integration by parts:

$$\delta F_s = \int_\Omega \mathrm{d}^3\mathbf{r} \left\{ \delta\psi^* \left[\alpha\psi + \beta|\psi|^2\psi + \frac{1}{2m^*}\left(\frac{\hbar}{i}\nabla + e^*\mathbf{A}\right)^2 \psi \right] + c.c. \right\} + \\ + \int_\Omega \mathrm{d}^3\mathbf{r} \left\{ \delta\mathbf{A} \left[\frac{\boldsymbol{\nabla}\times\mathbf{B}}{2\mu_0} + \frac{e^*}{2m^*}\psi^* \left(\frac{\hbar}{i}\nabla + e^*\mathbf{A}\right)\psi \right] + c.c \right\} + \\ + \int_{\partial\Omega} \mathrm{d}^2\mathbf{r} \left[\delta\psi^* \left(\frac{\hbar}{i}\nabla + e^*\mathbf{A}\right)\psi \right] \tag{1.2.15}$$

The last surface term is 'remainder' from the partial integration. The boundary condition can be satisfied through this term. This term is zero, if there is no current flow through the boundary:

$$\mathbf{n}\left(\frac{\hbar}{i}\nabla + e^*\mathbf{A}\right)\psi = 0 \tag{1.2.16}$$

The upper equations have to hold for every $\delta\psi^*$ and $\delta\mathbf{A}$. The resulting differential equations are the so-called Ginzburg-Landau equations:

$$\frac{1}{2m^*}\left(\frac{\hbar}{i}\nabla + e^*\mathbf{A}\right)^2\psi + \alpha\psi + \beta|\psi|^2\psi = 0 \tag{1.2.17}$$

$$\frac{1}{\mu_0}\boldsymbol{\nabla}\times\mathbf{B} = \mathbf{j} = -\frac{e^*}{2m^*}\psi^*\left(\frac{\hbar}{i}\nabla + e^*\mathbf{A}\right)\psi + c.c \tag{1.2.18}$$

Taking the first Ginzburg-Landau (GL) equation in zero magnetic field and assuming a homogeneous superconductor ($\psi \approx \psi_0$):

$$-\frac{\hbar^2}{2m^*}\nabla^2\psi_0 + \alpha\psi_0 + \beta|\psi_0|^2\psi_0 = 0 \Rightarrow |\psi_0|^2 = -\frac{\alpha}{\beta} \tag{1.2.19}$$

Using this result the $f = \frac{\psi}{\psi_0}$ dimensionless quantity can be introduced, and the equations can be written in the following form:

$$\xi^2\nabla^2 f + f - |f|^2 f = 0 \tag{1.2.20}$$

where $\xi^2 = -\frac{\hbar^2}{2m^*\alpha}$ is the characteristic length of spatial changes inside the superconductor, called the Ginzburg-Landau correlation length.

The penetration depth can be derived form the second GL-equation, which can be transformed into the form of Eq. 1.2.8 with a gauge transformation. The analogous expression is

$$\lambda_L^2 = \frac{m^*}{\mu_0 e^{*2}|\psi_0|^2} = -\frac{m^*\beta}{\mu_0 e^{*2}\alpha} \tag{1.2.21}$$

In inhomogeneous superconductors, where superconducting regions surround normal regions the magnetic field can enter the normal conducting region. In the superconducting region the magnetic field is zero, because it is shielded by the eddy currents on the surface of the superconducting domain. Expressing the magnetic field with the vector potential and using Stokes' theorem the flux flowing through the normal conducting regions is

$$\Phi = \oint_{\partial S} \mathbf{A}\,\mathrm{d}\mathbf{r} \tag{1.2.22}$$

where ∂S is a contour inside the superconducting region. The vector potential can be expressed from the second GL equation. Inside the superconducting region the contour of the integral can be chosen that way that the currents are zero, and the order parameter takes its equilibrium value with a phase factor, it can be assumed that $\psi = |\psi_0|e^{i\phi}$. Substituting this back to the second GL equation, the vector potential is proportional with the gradient of the phase. The expression of the flux is

$$\Phi = -\frac{\hbar}{e^*} \oint_{\partial S} \boldsymbol{\nabla}\phi \, \mathrm{d}\mathbf{r} \tag{1.2.23}$$

A full turn around the normal conducting region can change the phase by the multiple of 2π, finally it can be seen that the flux is quantized in e^* quanta.

$$\Phi = n 2\pi \frac{\hbar}{e^*} \tag{1.2.24}$$

To understand the formation of the Shubnikov phase, and derive an expression for the upper and lower critical fields, its important to derive the so-called vortex solutions of the GL equations. The $\kappa = \frac{\lambda}{\xi}$ Ginzburg-Landau parameter is an important measure of superconductors. For type-I materials $\kappa << 1$ for type-II materials $\kappa >> 1$. Using the $\psi = |\psi_0|e^{i\phi}$ ansatz the second GL equation takes the following form:

$$\mathbf{A} + \mu_0 \lambda_L^2 \mathbf{j} = -\frac{\phi_0}{2\pi} \nabla\phi \tag{1.2.25}$$

Integrating the upper equation on an arbitrary contour outside the vortex, and using Stokes' theorem:

$$\int_S \left(\boldsymbol{\nabla} \times \mathbf{A} + \lambda_L^2 \boldsymbol{\nabla} \times \boldsymbol{\nabla} \times \mathbf{B} \right) \mathrm{d}^2\mathbf{r} = n\phi_0 \tag{1.2.26}$$

It can be easily seen that the energetically optimal solution is when every flux line has only one flux quantum, so $n = 1$. In For type-II superconductors $\kappa >> 1 \rightarrow \lambda_L >> \xi$, which means that the spatial size of the normal conducting domain is much smaller then the characteristic variations in magnetic fields. In the $\xi \rightarrow 0$ case, the flux is enclosed into an infinitesimally thin line:

$$\mathbf{B} - \lambda_L^2 \boldsymbol{\nabla} \times (\boldsymbol{\nabla} \times \mathbf{B}) = \phi_0 \mathbf{z} \delta_2 (\mathbf{r}) \tag{1.2.27}$$

Where $\mathbf{z}$ is the unit vector in the z direction, which is the direction of the magnetic field and δ_2 is a two-dimensional Dirac-delta in the $x - y$ plane. Changing to cylindrical coordinates B_z can be expressed:

$$B_z - \frac{\lambda_L^2}{r} \frac{\mathrm{d}}{\mathrm{d}r} \left(r \frac{\mathrm{d}B_z}{\mathrm{d}r} \right) = \phi_0 \delta_2 (\mathbf{r}) \tag{1.2.28}$$

This is Bessel's equation with $n = 0$. The solution is

$$B_z = \begin{cases} \frac{\phi_0}{2\pi\lambda_L^2} K_0 \left(\frac{r}{\lambda_L} \right) & \text{outside the vortex} \\ \frac{\phi_0}{2\pi\lambda_L^2} K_0 \left(\frac{\xi}{\lambda_L} \right) & \text{inside the vortex} \end{cases} \tag{1.2.29}$$

From this the interaction energy of two parallel vortex can be calculated:

$$E_{12} = \frac{\Phi_0^2}{2\pi\mu_0\lambda_L^2} K_0\left(\frac{r_{12}}{\lambda_L}\right) \tag{1.2.30}$$

The interaction is repulsive, which dictates an equilibrium spatial distribution of the flux-lines which is called vortex lattice, which is a regular grid at low temperatures, but it can 'melt' if the temperature is higher, in the case of the high-temperature superconductors. Such a state state is called the vortex-glass state. The vortex-glass state is a quasi-equilibrium state is responsible for the magnetic relaxation.

With these results its easy to derive the expression for the upper and lower critical fields. For H_{c1} it can be assumed that the interaction between the vortices are negligibly small. In the net energy there is the positive vortex energy itself, and the magnetic field. The first vortex appears at H_{c1} field when the potential is zero:

$$G = E_{vortex} - \mathbf{BH} = 0 \tag{1.2.31}$$

For a sample with length L

$$LE_{vortex} = LH \int \mathbf{B} \mathrm{d}^2\mathbf{r} = LH\Phi_0 \Rightarrow H_{c1} = \frac{\Phi_0}{4\pi\mu_0\lambda_L^2} \ln\kappa \tag{1.2.32}$$

The number of vortices increases with the magnetic field; the magnetic field penetrates into the material gradually in form of vortices.

In the case of the upper critical field, when the mixed superconducting material completely goes into normal state, the order parameter is small, and the GL equations can be linearised. The result is the Schrödinger equation of electron gas in strong magnetic field:

$$\frac{1}{2m^2}\left(\frac{\hbar}{i}\boldsymbol{\nabla} + e^*\mathbf{A}\right)^2 \psi = -\alpha\psi \tag{1.2.33}$$

The resulting energy levels are the so-called Landau levels:

$$E = \frac{\hbar^2 k_z^2}{2m^*} + \left(n + \frac{1}{2}\right)\hbar\omega_c^* \tag{1.2.34}$$

With the assumption that $\alpha = \alpha_0 (T - T_c)$ is linearly dependent on the temperature, its value is negative below the critical temperature. The sign of α is chosen by the fact that the free-energy should have a minimum. Since

$$-\alpha \geq E_{min} = \frac{1}{2}\hbar\omega_c^* = \frac{1}{2}\frac{\hbar e^* B}{m^*} \tag{1.2.35}$$

The upper critical field is

$$H_{c2} = \frac{-2\alpha(T)\, m^*}{e^*\hbar\mu_0} \tag{1.2.36}$$

These results show that the critical fields are determined by only the α_0 and β phenomenological parameters, and the temperature.

1.3. The SuShi-septum project

The SuShi*(Superconducting Shield)*-septum project is a collaboration between CERN and Wigner Research Centre for Physics. Even though beam extraction from the FCC ring could be solved with current technology, a higher magnetic field is highly desired in order to make the system more compact. This would lead to cost savings in civil engineering (length of the tunnel), and it would be especially important in the high-energy LHC scenario (an alternative of the Future Circular Collider, with FCC technology installed in the LHC tunnel), where space would be extremely tight. Besides a high field, the apparent septum thickness (the total distance between the two beam channels, which includes the septum blade, vacuum pipes, etc) needs to be minimized in order to release the requirements on the kicker magnets' strength. These requirements clearly point towards superconducting solutions. In the SuShi-septum concept a passive superconducting shield would create a field-free region for the circulating beam within the bore of an exotic canted cosine theta-like magnet. The advantages of this configuration are as follows. (i) continuous 2D shielding current distribution, in contrast to the discrete wires of traditional (superconducting or normal-conducting) magnets. This gives perfect shielding up to a threshold field, depending on the shield's thickness. (ii) Absence of insulating material within the bulk shield material. This results in a better heat conductivity and better mechanical stability. (iii) As a result, smaller septum thickness than with other technologies.

2. Modelling of Superconductors

The Landau-Ginzburg theory presented in the previous section gives many answers about the phenomena experienced in the experiments with type-II superconductors, like how the magnetic field penetrates into the material in the Shubnikov phase. Several important questions were not discussed, like how the pinning centres and the vortices interact with each other, or the observed hysteretic behaviour of the materials. Furthermore, in numerical modelling for practical applications, it would be more beneficial to use some classical electrodynamics-based models, which describe the superconductor as a bulk medium with effective electrodynamic properties.

2.1. Critical State Model

The critical state model, or the Bean model [11, 12] can be intuitively introduced as follows. Changes in an external magnetic field will induce very high eddy currents in a very thin surface layer of the material. This, according to Lenz's law, will shield the interior of the magnetic field from the changes of the external field. However, since the induced current is higher than the critical current density of the material, the material will become normal conducting in this layer. Consequently, the current will decay, and the field will further penetrate into the material. When the current density reaches J_c, the critical current density, the material will become superconducting again, and the current will cease to further decay. Formulated differently, any electromotive force, whatever small, will induce J_c, the highest current density allowed in the superconducting state. The induced, steady eddy currents in the material are called persistent currents. The direction of the persistent currents depends on the direction of the electromotive force which was present at that region of the superconductor for the last time during the magnetic history of the material. The original Bean model assumed a critical current density which was independent of the magnetic field, and was useful to understand for example the hysteretic behavior of superconductors exposed to magnetic fields, or to qualitatively describe phenomena in idealized geometries. For the calculation of practical situations the model is insufficient. Also, the abrupt change of the persistent currents at the boundary between the zone penetrated by the magnetic field and the rest of the material is a further difficulty in numerical calculations.

2.2. Campbell's model

Campbell's model [14] starts from the experimental observation, that the force between the flux-lines and the pinning centres is elastic for small displacements and then it becomes a constant frictional force [13]:

$$f = BJ_c\left(1 - e^{-\frac{|s|}{d}}\right) \tag{2.2.1}$$

where d is a characteristic distance, and s is the displacement of a flux line. Furthermore, using the Weyl-gauge the electric field can be written as:

$$-\frac{\partial \mathbf{A}}{\partial t} = \mathbf{E} = \mathbf{B} \times \frac{\partial \mathbf{s}}{\partial t} \tag{2.2.2}$$

In a 2-dimensional problem $\mathbf{s}$ and $\mathbf{B}$ are in the xy plane and are perpendicular to each other, and every other vector point to the z direction. Using these, the magnitude of $\mathbf{s}$ is $s = -\frac{A}{B}$. Any motion of a flux line will result in a 'pulling back' force by the pinning centre with the magnitude of Eq. 2.2.1, and points in the opposite direction. The flux lines can be moved apart from their pinning centre only by the Lorentz force. In the stationary case their magnitude is equal:

$$BJ = -BJ_c \left(1 - e^{-\frac{|s|}{d}}\right) \tag{2.2.3}$$

Considering that between negative and positive displacements the force on the right-hand side changes signs, the upper equation can be expressed in the following way:

$$\boldsymbol{\nabla} \times (\boldsymbol{\nabla} \times A_z) = -\mathrm{sgn}\,(A_z)\,\mu_0 J_c \left[1 - \exp\left(-\left|\frac{A_z}{Bd}\right|\right)\right] \tag{2.2.4}$$

Expanding the double curl operator we get

$$\boldsymbol{\nabla}^2 A_z = -\mathrm{sgn}\,(A_z)\,\mu_0 J_c \left[1 - \exp\left(-\left|\frac{A_z}{Bd}\right|\right)\right] \tag{2.2.5}$$

This is a non-linear implicit second-order PDE, which can be relatively easily solved numerically if the Bd term is not too small. It can be easily seen that the transition between $+J_c$ and $-J_c$ is smooth, and the Bd constant controls the thickness of the transition zone. This constant is usually noted as A_r. The J_c value can be dependent on the magnetic field, for example, it could have an exponentially decaying characteristics.

Campbell's model is a static model, which directly calculates the steady state resulting from a time-dependent dynamic process: the direct magnetization of a superconductor from the "virgin state" (where the superconductor has not yet been exposed to a magnetic field before). The virgin state is reached when the superconductor is cooled below T_c in zero external field. The resulting magnetic state is an approximation of Bean's critical state, in which the transition between the magnetized and non-magnetized zones of the superconductor are smoothed. Being static, the finite-element implementation of the model runs very fast, and it is therefore adequate for parameter scans or parameter optimization. However, it can not describe time-dependent problems (like relaxation), and magnetic field ramps with changing direction (i.e. hysteresis).

2.3. Eddy Currents with non-linear E-J curve

Several experiments have observed that the magnetic dipole moment of most of the superconductors decays with time. This phenomenon is called magnetic relaxation. Different theories suggested that this happens because of the relaxation of the supercurrents. This sounds like

a contraindication with the lossless conducting properties of the superconductors, but actually, these are not resistive losses like in the case of regular materials.

In 1964 Anderson and Kim gave a simple possible explanation of this phenomenon [16]. From the interaction force between individual flux lines they have deducted the fact that the arrangement of the flux lines can be irregular on scales larger than the penetration depth, otherwise it would be energetically really unfavourable. Because of this, the flux lines are 'clustered' into so-called flux-bundles the radius of which is on the scale of the penetration depth. Inside these bundles the organization of the distinct flux lines is regular. There are barriers between the flux bundles the energies of which can be calculated. Depending on this energy, there is a specific rate of the individual flux lines jumping through the barrier out from the bundle due to thermal activation. This thermal activation of flux line causes the rearrangement of the vortex-glass structure inside the material which can cause the relaxation of the critical currents.

A result of the Anderson-Kim theory [16] is that the barrier energy between the flux bundles has a linear dependence on the current density:

$$U = U_0 - \frac{JBx_0V}{c} = U_0\left(1 - \frac{J}{J_{c0}}\right) \tag{2.3.1}$$

where V is the volume of the flux bundle, x_0 is the hopping distance and $J_c = \frac{cU_0}{Bx_0V}$ [17]. The velocity of a thermally activated flux line is proportional with the probability of the hopping:

$$v = v_0 e^{-\frac{U(J)}{k_B T}} \tag{2.3.2}$$

Since $E \propto vB$. Using Eq. 2.3.1 and Eq. 2.3.3 a relationship between E and J can be derived:

$$E \propto B \exp\left[-\frac{U_0}{k_B T}\left(1 - \frac{J}{J_{c0}}\right)\right] \tag{2.3.3}$$

It can be shown that an exponential dependence in the $E-J$ characteristics causes a logarithmic magnetic relaxation [17]. The Anderson-Kim model works well if $U_0 >> k_B T$ which is not the case for high-temperature superconductors. There are several models explaining these cases with non-linear barrier energies used.

Another possible $E - J$ characteristics of superconductors can be introduced in a very intuitive and qualitative way. For superconductors there is no electric resistance until a specific critical current is reached. After this point is reached, the resistance will have a finite value. Typically, such abrupt changes cause convergence problems in FEM models. This behaviour can be approximated with a smooth power-law-like characteristics:

$$E = E_0\left(\frac{J}{J_c(B)}\right)^n \tag{2.3.4}$$

where $J_c(B)$ is the magnetic field dependent critical current density of the specific superconducting material which can be modelled or determined from measurements, and n is a phenomenological parameter. This model gives back the true critical state if n is chosen as infinite. With a

finite but large n this model both gives the approximation of the critical state model, and introduces relaxation phenomena (i.e. losses below J_c). In certain cases the quickly diverging electric field must be limited by adding a finite-resistivity component in parallel to the pure power-law curve [18]. This has a really intuitive interpretation: after the superconducting state is ruined by the large currents, the material acts as a regular linear resistivity. The corresponding modified power-law has the following:

$$E = \frac{\rho_n E_0 \left(\frac{J}{J_c(B)}\right)^n}{E_0 \frac{J^{n-1}}{J_c(B)^n} + \rho_n} \tag{2.3.5}$$

where ρ_n is the normal state specific resistivity. With these conduction relations, the numerical study of superconductors is just like that of regular materials.

2.4. Numerical Study of Partial Differential Equations

The laws of nature are described mostly by partial differential equations. Unfortunately only a small fraction of these equations can be solved analytically without any approximations in specific cases, and an even smaller set of them can be solved in a general case. Due to these reasons, the numerical study of differential equations is an extremely important field both in science and in industry. Almost every aspect of our modern technology is related to this field, starting from the design of a radio antenna through the aerodynamic optimization of a car to the fatigue calculations of support structures. Mainly three different approaches are used to produce a numerical representation of PDEs; the finite difference, the finite volume, and the finite element method. Each one has advantages and disadvantages.

The finite difference method replaces the derivatives in the equations with differences over a spatially discretized grid. It is usually really easy to implement, and because of its simplicity, very efficient codes can easily be developed for simple, regular geometries. Its accuracy can be easily increased by refining the discretization. Unfortunately the implementation of this method gets extremely hard for complex geometries, mostly because the derivatives in an equation is calculated in the ordinary directions of an ordinary coordinate-system. To handle complex geometries, conformal mappings could be used to map the irregular grid into a regular one, but usually its hard to find such mappings, and even simple linear equations could easily become highly non-linear.

The finite volume method is more suitable for the study of complex geometries. It divides the model spatially into small volume elements, and requires the satisfaction of different conservation laws between the volume elements. Due to its working principle, this method is very successful in CFD and heat transfer simulations, where the PDEs have to be solved are basically conservation laws. The industrial standard ANSYS Fluent commercial CFD package is based on this method.

The last method is called the finite element method. This is the most widely used method in industry. It divides the model into small elements, which can be irregular, like tetrahedrons. It

is based on the so-called weak formulation. Calculus of variations says that solving the operator equation

$$\hat{A}u = f \tag{2.4.1}$$

where u is an element of a Banach space $\hat{A}$ is an operator mapping from the Banach space to its dual is equivalent with finding such u that

$$[Au](v) = f(v) \tag{2.4.2}$$

$\forall v$ where v is called 'weighting function' the element of the same Banach space as u. The $[Au](v)$ functional can be 'produced' for example by the inner product. Using the upper statement for differential operators, making the Banach space to a Hilbert space, the problem is the following:

$$\int \left(\hat{A}u\right) v = \int fv \tag{2.4.3}$$

Here v can be chosen arbitrarily. For practical reasons they are usually functions with finite support, which is the upper mentioned 'small element', for example a piecewise linear function, which is zero everywhere, except inside the finite element. Let n be the highest order of derivative in the $\hat{A}$ operator. This way the solution must have at least n continuous derivative, otherwise the integrals might not be defined in Riemann-sense. Integrating by parts, the order of derivatives present in the differential operator, could be reduced by one, so the solution is required to has only $n-1$ continuous derivatives. In this sense, the condition for the derivatives is weakened, this is why this form is called the weak form of the equation. For example, for Laplace's equation in 1D we get

$$\int_a^b \frac{\mathrm{d}U(x)}{\mathrm{d}x}\frac{\mathrm{d}v_i(x)}{\mathrm{d}x}\,\mathrm{d}x - \left[v_i(x)\frac{\mathrm{d}U(x)}{\mathrm{d}x}\right]_a^b = \int_a^b 4\pi f(x)\, v_i(x)\,\mathrm{d}x \tag{2.4.4}$$

The integration is over a single finite element. The second term in the left hand side is zero, because the weighting function vanishes on the boundaries. So far this is completely equivalent with the original differential equation. The weighting functions are indexed because they are non-zero only over the ith finite element. Since the elements are not overlapping, the weighting functions over the elements can be used as a basis on our Hilbert space, on which we can expand our solution:

$$U(x) = \sum_i^\infty \alpha_i v_i(x) \tag{2.4.5}$$

The approximation is when we don't use an infinite number of base elements for this expansion, but only a finite number. If the weighting functions are constructed from for example linear or quadratic polynomials, the integrals can be easily evaluated analytically over the finite element, leaving only the α_i expansion coefficients as unknown. Calculating this for every finite element results in a set of linear equations, which can be solved either by a direct or an iterative method.

3. Experimental Results

The measurements have been performed in CERN's SM18 cryogenic facility. The superconducting materials were mounted into a spare LHC dipole corrector magnet (MCBY) [7]. The magnet with the shield was cooled down to either 4.2 K or to 1.9 K using liquid helium. Different coil current profiles were used in order to study the maximal shielding capability, relaxation, and magnetization properties of the two tested materials. I have participated in the planning, preparations, assembly and measurements of the NbTi/Nb/Cu test setup. Experimental results of the MgB_2 shield are summarized for the better understanding of the numerical results, presented in a later chapter of this thesis.

3.1. MgB_2 tube

Magnesium-diboride is a high-temperature superconducting material with $T_c \approx 39K$ critical temperature. It was one of the candidate materials because of its relatively low price. The tube we have used was produced by Giovanni Giunchi by reactive Mg infiltration [19]. In this process, a boron preform was first produced by compressing crystalline boron powder around a solid central magnesium rod, inside a steel container. A boron grain size of 160 μm was chosen since it demonstrated better stability against flux jumps in earlier experiments [20]. The container was sealed by welding and then heated up in an oven. The molten magnesium penetrates the boron preform and reacts with it. The steel container counteracts the pressure and results in a high-density material. The tube had a length of 450 mm, an outer diameter of 49 mm and a wall thickness of 8.5 mm.

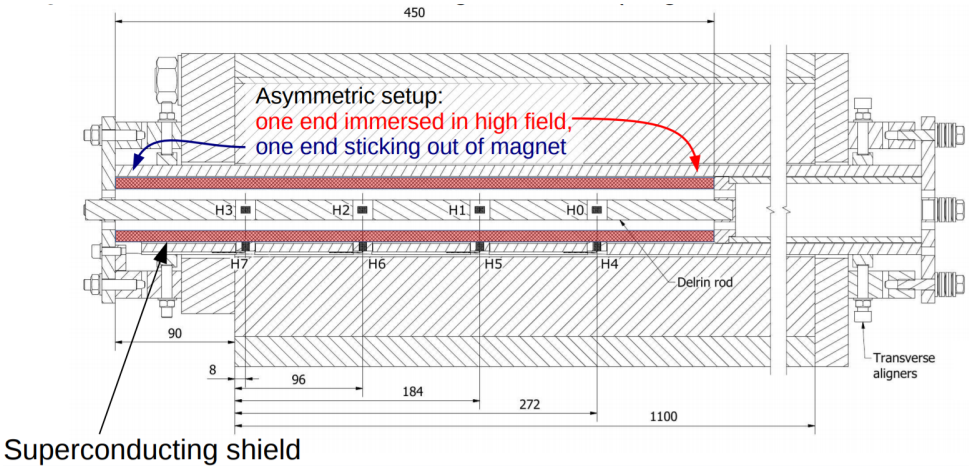

Figure 3.1: The experimental setup of the MgB_2 tube [22]

Four Hall sensors were mounted outside of the shield, with their sensitive area about 2.5-3 mm away from the shield's external surface. Four other Hall sensors were mounted onto a delrin

rod, which was inserted into the centre of the shield. All sensors were aligned parallel to the external field. Figure 3.1. shows the position of the sensors.

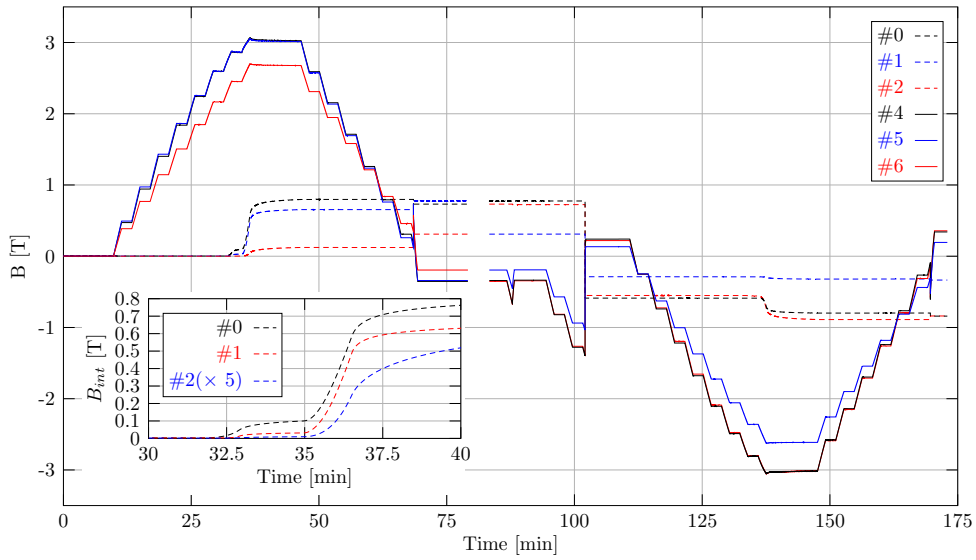

Figure 3.2: The full current cycle

Figure 3.2 shows the magnetic field measured by the internal and external Hall sensors as a function of time in a full measurement cycle. The magnet current was linearly ramped with a rate of 0.1 A/s for 95 seconds (this corresponds to about 3.5 mT/s field ramp rate in the empty magnet), and then kept constant for 120 seconds in order to study the relaxation of the shielding currents at different field levels. The results of Hall sensors #3 and #7 are not shown since they were in the fringe field of the magnet, measuring a much smaller magnetic field which is not interesting for this experiment. The field started to fully penetrate at about 2.7 T measured by the external Hall sensors. According to a 2D finite-element simulation, this corresponds to about 2.9-3 T directly at the shield's surface. The study of relaxation is important for two reasons. (i) The slow decrease of the field outside of the shield introduces a time-dependence of the system, which must be compensated for example by appropriately increasing the magnet current. The magnitude of this effect is a function of not only the superconductor's parameters but also of the particular geometry of the setup and the position of the field measurements. A long-term measurement (Fig. 3.3) confirmed that the total relaxation of the external field is about 0.25 % over 6 hours for a field level of 2.4 T, which is acceptably small. (ii) If the shield is running close to its limits, relaxation can finally lead to the field penetrating to the interior of the shield, which is not acceptable in this application.

Even though the shield was stable against flux jumps on the virgin curve, it did suffer from flux jumps at low fields after it had been exposed to high fields before (big jumps in Fig. 3.2). This would necessitate the thermal reset of the shield (heating above T_c and cooling back in zero

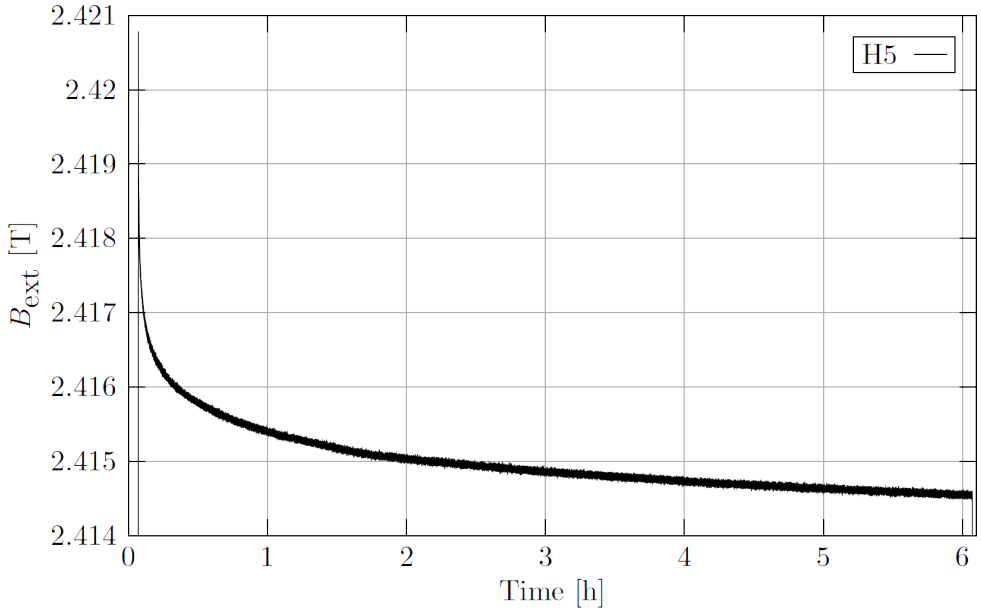

Figure 3.3: Long term relaxation of MgB_2

field) between accelerator cycles, which would lead to too much dead time. Another difficulty is the production of long (about 2 m) tubes, for which the superconducting joining technique [21] might provide a solution.

Figure 3.4 shows the external field measured by the sensor H4 as a function of magnet current in the same measurement cycle as presented before, compared to a simulation assuming an ideal diamagnet shield. The departure from linearity is due to the increasing penetration depth of the field at high currents, which leads to the effective shielding surface drifting inwards. This causes a decreasing field concentration at the position of the Hall sensor, compared to the linear behaviour.

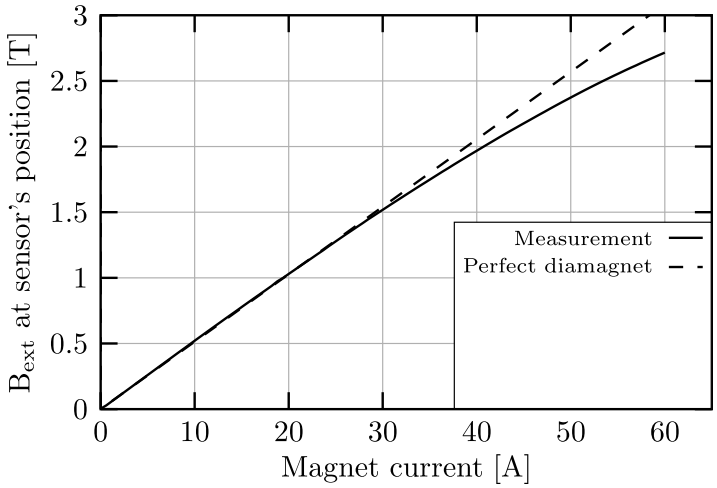

Figure 3.4: Non-linearity of MgB_2

3.2. NbTi/Nb/Cu multilayer sheets

NbTi/Nb/Cu is a superconducting material developed by I. Itoh and T. Sasaki at Nippon Steel corporation in 1993 [23, 24]. These sheets consist of multiple layers of niobium-titanium, niobium and copper. Multiple sheets of precursor materials are layered in a copper box, which is then electron beam welded under vacuum. It is then hot rolled, cold rolled and heat treated in several steps. The 0.8 mm thick finished multilayer sheet contains 30 layers of NbTi with a thickness of 0.9 μm.

The experiments with this material were performed in March 2018 in CERN's SM18 facility. A cylinder of length L=450 mm, inner/outer diameter 41/47.4 mm was constructed from two half cylinders, each consisting of 4 layers of a 0.8 mm thick NbTi/Nb/Cu multilayer sheet shown in Fig. 3.5 (c).

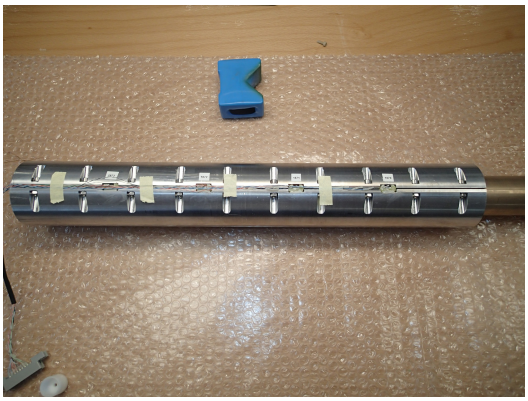

(a) Al clamps with external Hall sensors

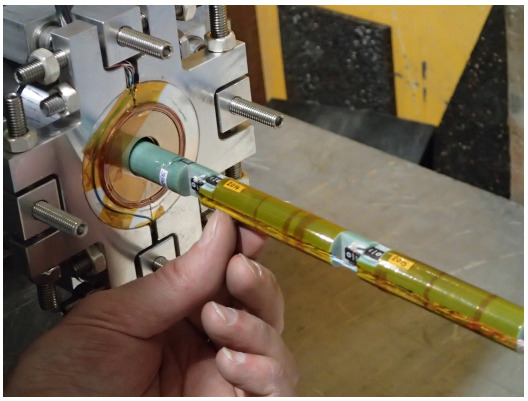

(b) Delin rod with inner Hall sensors

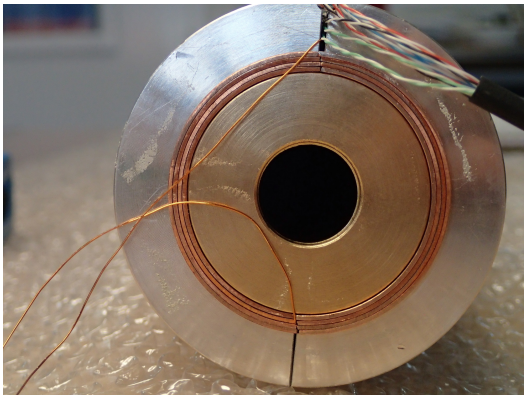

(c) Cuts on the multilayer sheets

Figure 3.5: Experimental setup for the NbTi/Nb/Cu multilayer

Figure 3.6 shows different cylindrical shield configurations for a transverse dipole field which can be made from a sheet material. With two half cylinders aligned perfectly with respect to the external field (a) the shielding currents do not cross the plane of the cut, and the leaking magnetic field inside the shield is perpendicular to the external field. If the shield is misaligned

(b), induction lines can pass through the two cuts and the major component of the leaking field will be perpendicular to the external field. This effect is eliminated and the sensitivity of the shielding efficiency to the alignment is suppressed if the shield is made from concentric C-shape elements as shown in Fig. 3.6(c). Even though the configuration (c) was planned initially, the sheets were accidentally cut to half without excess material, which finally only allowed the realization of the two half-cylinders configuration, without the possibility to machine the meeting sides of the half cylinders to a flat surface. This resulted in small gaps between the two half-cylinders. In addition, they could not be perfectly aligned during the assembly. The cuts in the different layers had slightly different orientations, also varying with the axial position.

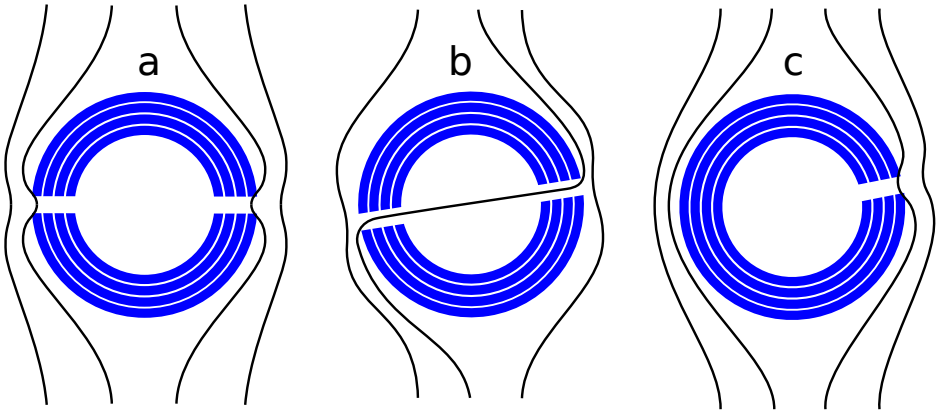

Figure 3.6: Different cylindrical shield configurations made from a sheet material

The half cylinders were clamped between a bronze tube support (ID/OD=18/41 mm) and half-cylindrical aluminium clamps, as shown in Fig. 3.5 (a), Fig. 3.5 (c). Hall sensors (Arepoc HHP-NP) were installed into slots of the aluminium clamps to measure the external magnetic field, with a parallel orientation. The same type of Hall sensors were mounted to a delrin rod, which was inserted into the bronze support tube. These sensors were aligned both parallel and perpendicularly to the external field. The experimental layout is shown in Fig. 3.7, which also shows the numbering of the sensors. A thin pickup coil was installed around the shield along the cuts on both sides, in the gap between the two aluminium clamps. Unfortunately, a part of this coil was stuck between the clamps and shorted the circuit. This half was cut out and replaced by a wire taped to the outside surface of the clamps in the midplane. The purpose of this coil was to pick up sudden changes of the external magnetic field in case of a flux jump, measure its time difference with respect to the signals of the internal Hall sensors, and ultimately to evaluate the feasibility of this method as an early diagnostics of flux jumps, to safely abort the beam before the penetrating field has fatal consequences.

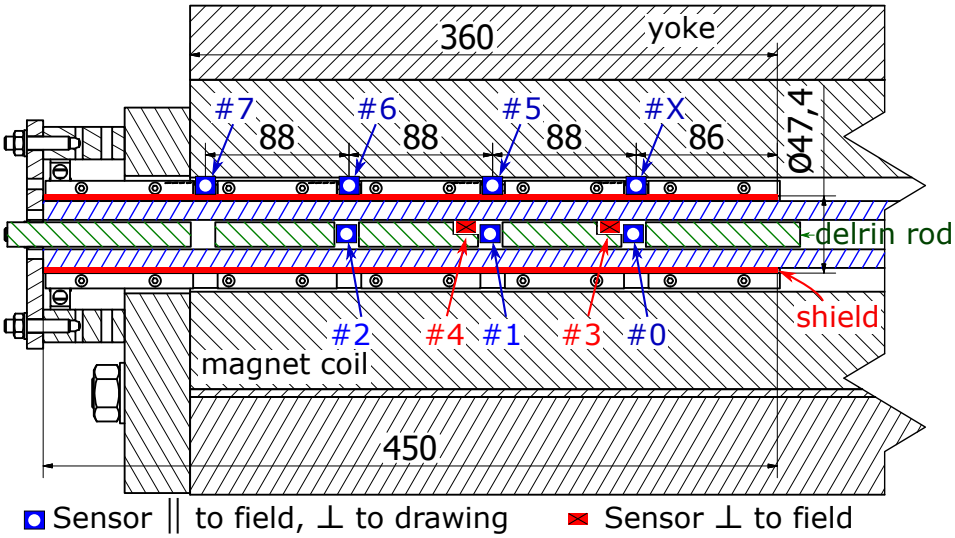

Figure 3.7: The Hall sensors layout of the NbTi/Nb/Cu multilayer experiment

The #7 Hall sensor was in the fringe field of the magnet; it was measuring zero field almost all the time, so its signal is not shown. The soldering on the external sensor after #5 (noted as #X) was sticking out, had only about 0.2-0.5 mm play in the magnet and broke down during the mounting of the shield, which is unfortunate since it was the farthest external sensor from the fringe field. The active spot of the external Hall sensors was about 2.5 mm away from the outer surface of the shield. A short 'calibrating' measurement was done with a single ramp to 10 A coil current at 4.2 K temperature. The results are shown in Fig. 3.8.

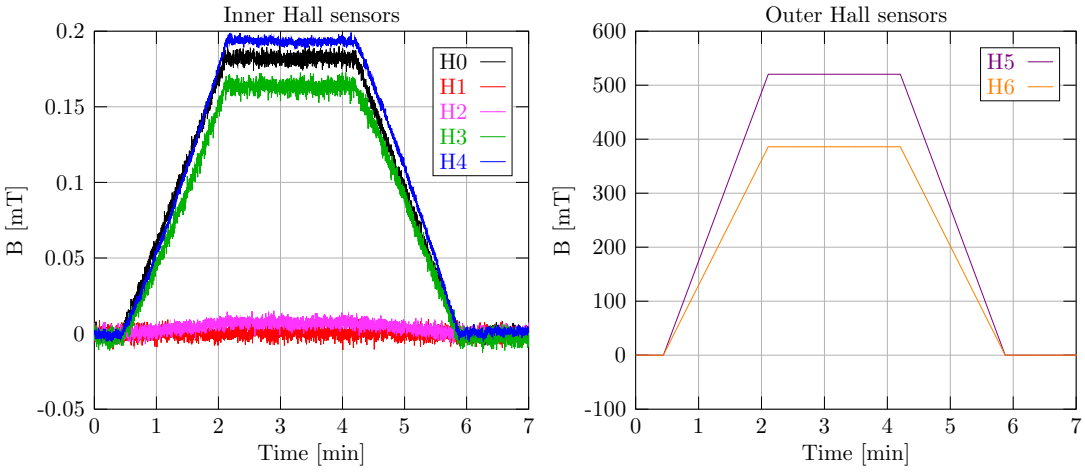

Figure 3.8: Sanity-check measurement on NbTi/Nb/Cu multilayer with 10A coil current

The lower value measured by H6 is due to it being already in the fringe field region of the magnet. The H3 and H4 sensors are measuring the horizontal field inside the shield. The H1 and H2 sensors are measuring the vertical field*(the direction of the dipole field generated by the*

magnet), which is much smaller than the horizontal. This supports the previous statement that the magnetic field penetrates through the gap resulting in a horizontal inner field. The vertical field inside is non-zero because the cuts on the left and the right side of the shield are not exactly on the same level.

The H0 sensor also measures the vertical field which is higher than the horizontal field at this point. This seems like a contradiction with the previous statement, but actually, this high vertical field is caused by the end-effect. This Hall sensor is near the open end of the shield, at a distance comparable to its inner diameter, i.e. the characteristic penetration depth of the field through the open end. This effect was also experienced with the MgB_2 tube. Since the measured magnetic field at the inner parts of the shield is small, we can safely say that the shield is performing well.

After the installation and cool-down of the setup initial tests of the magnet, its power supply and quench protection system were carried out, which included fast ramp-ups of the magnet current, and fast energy extraction. These have lead to flux jumps in the shield, or the quench of the magnet, which in turn induced a flux jump in the shield. This measurement of the shield was carried out starting from this non-virgin state, with the trapped magnetic field in the shield, due to the preliminary tests of the current generator, and Hall sensors. The results are shown in Fig. 3.9.

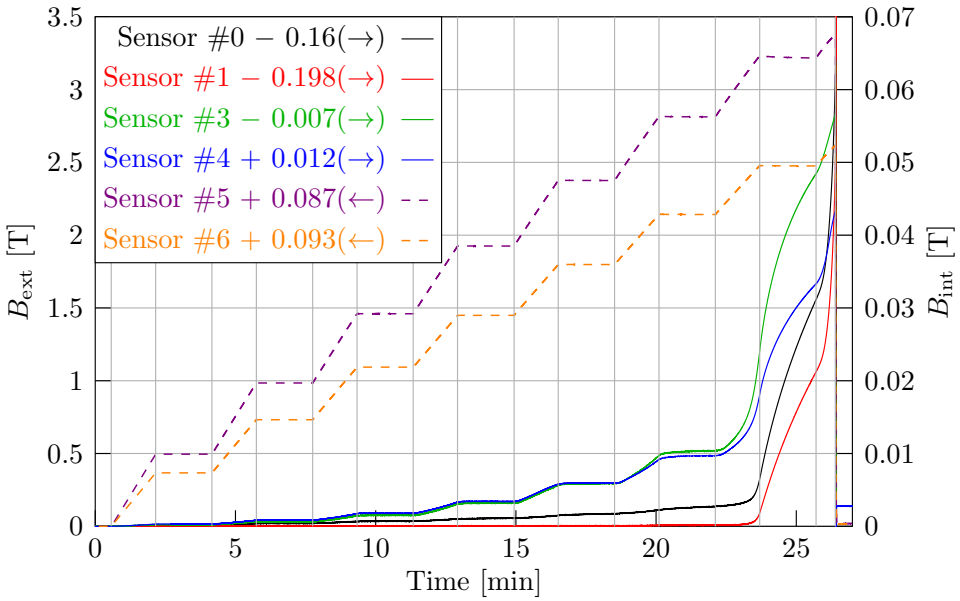

Figure 3.9: Measured inner and outer magnetic field after the subtraction of the trapped field

The signal of H0 and H1 start strongly but smoothly rising after the plateau before the last one, right after 22 min. The field measured by H5 is 3.15 T, the coil current at this point is 64.75 A. After this point the magnetic field completely penetrates inside the shield even when the next plateau is reached and the external magnetic field stops rising. Because of this, the

last stable plateau is the previous one (the 6th), starting at around 20 minutes. The external magnetic field at this plateau is ≈ 2.81 T 2.6 mm away from the shield's surface, which means ≈ 3.1 T field directly at the surface. This is similar to the performance of MgB_2, but with a wall thickness less than half of that of the previous construction, and the measurement has started from a non-virgin state which introduces some uncertainty of this specific measurement. The further increase of the magnetic field has led to a flux jump, visible at ≈ t = 26 min.

In order to eliminate the trapped field from the shield, it was warmed up above its critical temperature. The signal of the Hall sensors was monitored during the warm-up, and clearly indicated the transition of the shield to normal-conducting state. The temperature shown by the sensors attached to the magnet was around 50 K when cool-down in zero field started again. Even though electric heaters were attached to the magnet, the complete cycle took almost 24 hours due to the long time needed to evaporate liquid helium from the large cryostat, and the large heat capacity of the 1.2 tons magnet. Testing the shielding limits of the superconducting shield starting from a virgin state would have led to another full penetration and the loss of another 24 hours due to the subsequent thermal reset cycle. Due to the limited time for the experiment, this test was omitted and following measurements were limited to a magnet current of 55 A, slightly below the value at the last stable plateau (57 A), hoping that this is still below the penetration limit when starting from a virgin state.

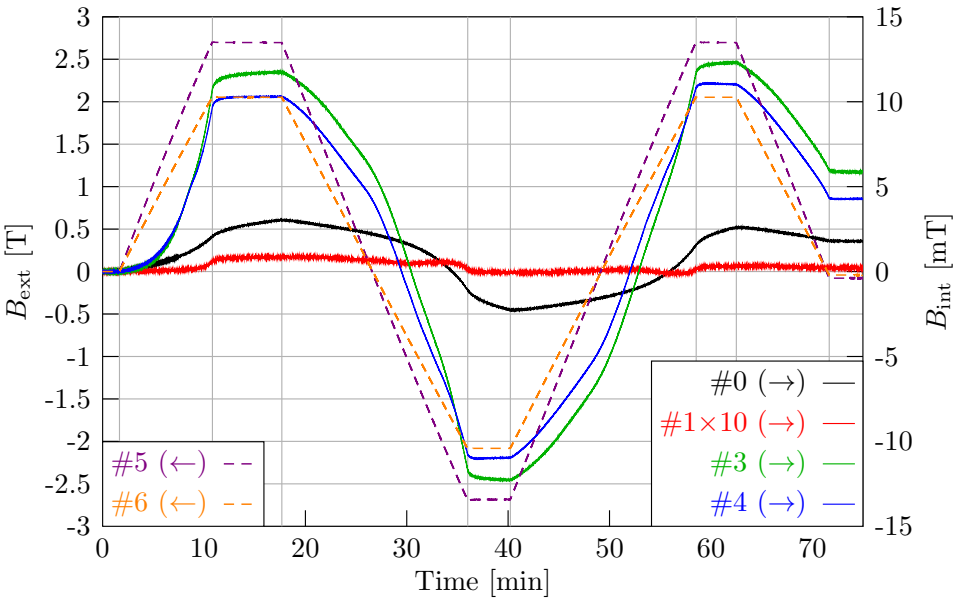

Figure 3.10: Measured inner and outer magnetic field in the case of 55 A cycle

Figure 3.10 shows the magnetic field measurements during a cycle between ±55 A, starting from the virgin state. At the highest current the external magnetic field measured by the sensor #5 was 2.7 T. This corresponds to a magnetic field of about 3.1 T directly at the shield's surface. Among the internal Hall sensors the ones with perpendicular orientation (#3 and #4)

measured by far the largest field, up to about 12.5 mT. This corresponds to an attenuation of about $4.6 \cdot 10^{-3}$. Sensor #0, oriented parallel to the external field, measured only about 3 mT, corresponding to an attenuation of about 10^{-3}. Field leakage of this orientation at this position is due to the end effect. Inner sensor #1 measured a magnetic field only below 0.1 mT (which corresponds to an attenuation of $4 \cdot 10^{-5}$, already acceptable for the intended application). At the end of the cycle, both the external and the internal (#0, #3, #4) sensors show the presence of a magnetic field which was trapped.

Figure 3.11 shows the inner magnetic field as a function of magnet current.

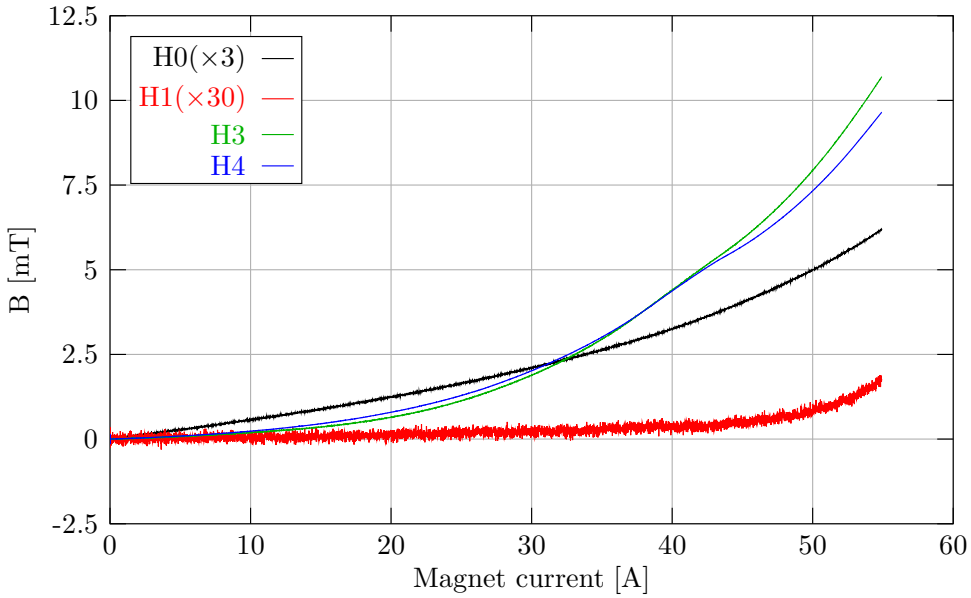

Figure 3.11: Non-linear increase of horizontal magnetic fields inside the shield

The signals of H0 and H1 (the vertical sensors) are small and start linearly. This is due to the fact that their distance from the open end is much larger than the penetration depth of the magnetic field into the bulk material, the penetration through the shield, therefore the nonlinear effects of the distortion of the field pattern are negligible. The signals are simply proportional to the external field.

The H3 and H4 sensors are showing non-linearly increasing magnetic fields. This signal can be described by two different effects. First, the external magnetic field increases linearly, which causes the linear increase of the leaking field through the gaps for small external fields, and second, the penetration of the magnetic field inside the material, which leads to a virtual increase of the gap size. This phenomenon will be detailed in the numerical section.

Following this cycle, the shield was cooled down to 1.9 K without thermal reset. The current was ramped up linearly to 38, 47.5, 55, 57, 59 A. The results are shown in Fig. 3.12. For sensor #1 the variation during the plateaus was 0.01 mT during the whole cycle before the flux jump. The shielding performance is better, and the relaxation is almost negligible. This reflects the

smaller relaxation of the shielding currents and the larger critical current at lower temperatures.

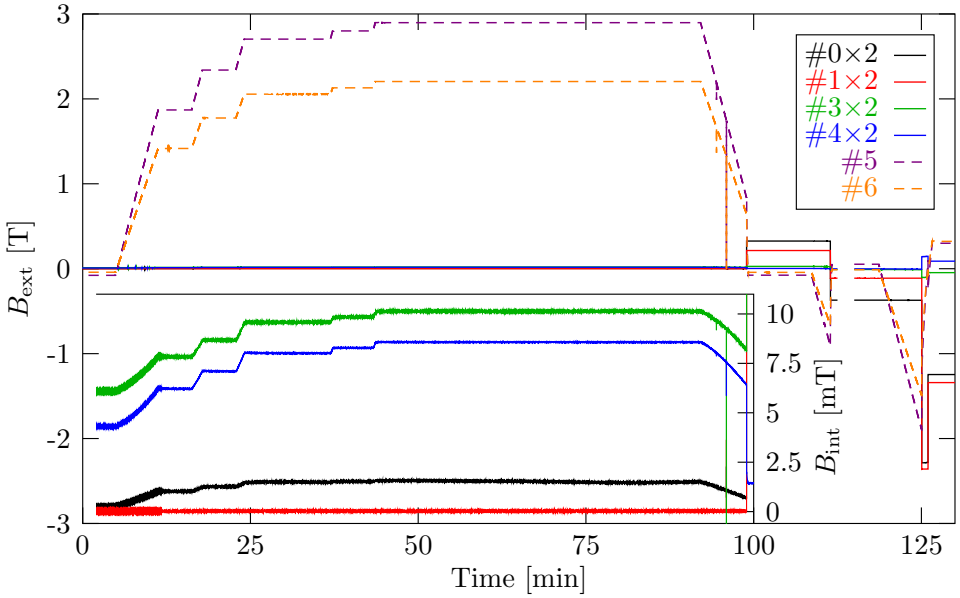

Figure 3.12: Measured inner and outer magnetic field

Rather than testing the ultimate shielding limit at 1.9 K, the magnetic field was ramped down to zero, in order to test the shield's stability during a full magnetic cycle, which is of crucial importance for the shield's application in a septum magnet. A flux jump occurred when approaching zero field, and further cycles were hindered by persistent flux jumps. This behaviour is similar to that observed with the MgB_2 shield. Due to the shield's instability against flux jumps, application at 1.9 K is therefore not possible.

To trigger the emergency beam abort in time, it is necessary to detect a flux jump before the magnetic field penetrates into the shielded region. Since the material was quite stable at 4.2 K, the flux jump was preceded by the smooth penetration of the field. Given the apparent stability of the shield against flux jumps at the intended field levels, in a realistic scenario an eventual flux jump would be caused by an external perturbation. In this case, a flux jump would occur directly from a perfectly shielding state. In order to trigger a similar situation, the measurement was performed at 1.9 K. The results are shown in Fig. 3.13. The peak in the pickup coil's signal precedes the signal of #5 by ≈10 ms and by ≈15 ms the #1 signal. This time interval seems to be safe to trigger the emergency beam abort in the ring.

Since the superconducting shield is a passive device, its magnetic state is not a direct function of the externally controlled parameters like the magnet current. It depends on the magnetic history of the device, which necessitates extra measures to ensure that the shield is in a defined state, and the field inside and outside of it are as expected. In case of a flux jump, the field penetrates to the interior of the shield. Besides the immediate beam abort, the shield needs to be heated above T_c and cooled back in zero field ("thermal reset") to eliminate the trapped

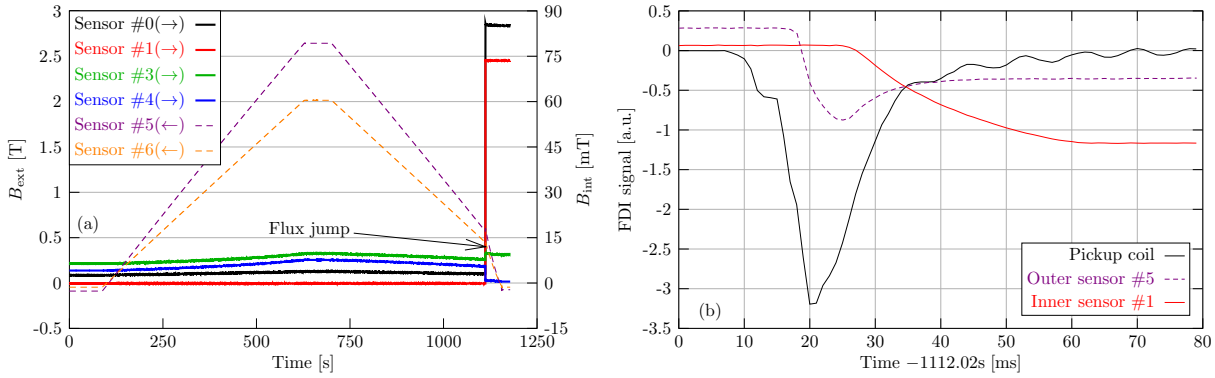

Figure 3.13: Measured signals during quench

field. This cycle takes long, so flux jumps are to be avoided at any cost. However, even without a flux jump, a trapped magnetic field will remain in the thick wall of the shield after a high field exposure. The trapped field will distort field homogeneity, most significantly at low external field levels, i.e. an injection into the ring. If this can only be done with a thermal reset cycle, it would cause unacceptably long deadtimes between accelerator cycles. A demagnetization cycle was performed to demonstrate that the effect of the field trapped in the thick wall of the shield can be eliminated without a thermal reset cycle. The results are shown in Fig. 3.14. The magnet current was ramped to 54 A and then back to zero. This corresponds to the solid black line O-A-B in Fig. 3.14b. At zero current the trapped field at the position of the Hall sensor #5 was 75 mT. The second ramp to 54 A (green dotted line B-A) had a trace different from the virgin curve but reached the final endpoint A as before, illustrating the effect that exposures to fields at least as high as the highest level reached before erase the magnetic history of the shield. A double-ramp to -54 A and 54 A traced the full, symmetric hysteresis loop (red dashed line A-C-A). A final degaussing cycle with alternating polarities and decreasing amplitudes (solid blue line A-D-E-F-G-O) brought the shield back to the same effective magnetic state O as the starting point.

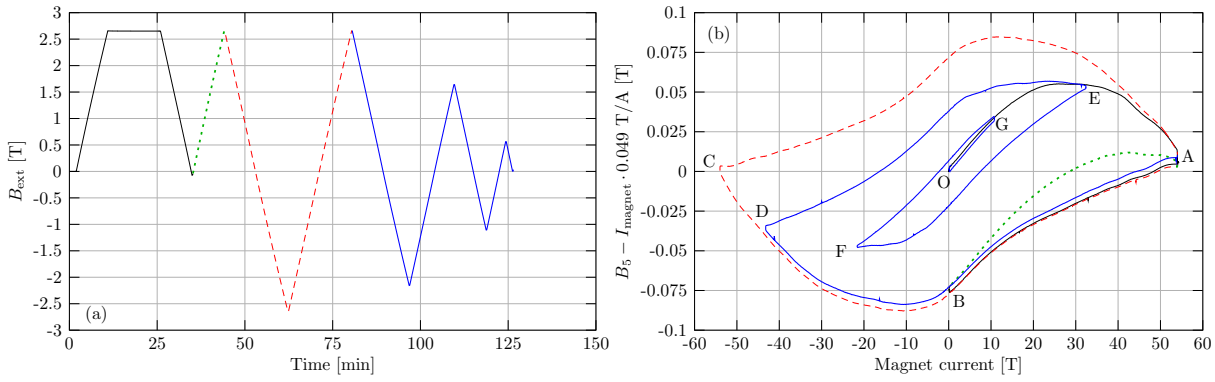

Figure 3.14: Demagnetization of NbTi/Nb/Cu multilayer

4. Numerical Results

This section is for the presentation of the numerical explanation of the experimental results for both tested materials. The simulations have been performed with a commercial finite element software, COMSOL Multiphysics 5.2a. Two different approaches were used, one is the *'Magnetic Fields'* physics, which solves Maxwell's equations in the vector potential formalism, which makes it capable to compute magnetic fields and induced current distribution, especially in 2D. The other was the *'Magnetic Field Formulation'* physics which solves Maxwell's equations using the magnetic field as the dependent variable. It is mostly used if the previous approach is not applicable, for example the time-dependent modelling of materials with strongly non-linear E-J characteristics, like superconductors. The software comes with a built-in simple CAD model builder. Each of the presented geometries was built with this model builder.

4.1. Relaxation phenomenon in MgB_2

To reproduce the experimental results presented in Section 3.1, first Campbell's model was used to perform a quick parameter estimation for the $J_c(B)$ characteristics of the material, which was assumed to take the following form:

$$J_c(B) = J_0 e^{-\gamma B} \tag{4.1.1}$$

Here both J_0 and γ are phenomenological parameters, which need to be determined either numerically, or experimental $J_c(B)$ curves could be used. The J_0 parameter controls the maximal current density the material can carry, and γ controls the steepness of the degradation of the critical current due to larger magnetic fields. From Campbell's model, the following current is prescribed to flow in the bulk material:

$$J_{Cb} = -J_c(B) \tanh\left(\frac{A_z - A_0}{A_r}\right) = J_0 e^{-\gamma B} \tanh\left(\frac{A_z - A_0}{A_r}\right) \tag{4.1.2}$$

Following the arguments in [15], the function $-\mathrm{sgn}(A_z)\,\mu_0 J_c\left[1 - \exp\left(-\left|\frac{A_z}{Bd}\right|\right)\right]$ has been replaced by $\tanh\left(\frac{A_z - A_0}{A_r}\right)$ for convenience. The parameter A_r defines the size of the smooth transition zone between magnetized and non-magnetized zone.

In the vector potential formulation, the dependent variable is the vector potential. All other quantities are derived from this. The magnetic induction ($\mathbf{B}$) is the curl of the vector potential, therefore at least second order finite elements must be used, otherwise $\mathbf{B}$ would be element-wise constant even when the solution in $\mathbf{A}$ is continuous. Furthermore, additional requirements can be introduced for the mesh size, based on the gradient of the solution near the boundaries of the finite elements. The solution in the two elements has to fit continuously, so the solution cannot be arbitrarily small in one element if it has a non-zero slope at the boundary of the neighbouring

element. Due to this near large gradients overshoots of the solution can be experienced, which can be eliminated by a sufficiently small mesh size.

In our case, the prescribed currents in the shield determines the vector potential. The steeper the transition between $-J_c$ to $+J_c$ the finer mesh is required to resolve the boundary between the zero-field and the penetrated region in the bulk material. Quantitative criteria could be given to the maximum size of the mesh element, but since solving Campbell's model is extremely fast, multiple mesh sizes were tested, and the mesh size on which the solution did not have the upper mentioned periodic overshoots was accepted as a sufficiently small one. The geometry and the mesh are shown in Fig. 4.1. Due to symmetry reasons, only a quarter of the whole magnet was modelled. The boundary conditions (BCs) were

$$\mathbf{n} \times \mathbf{H} = 0 \qquad \text{in the horizontal symmetry plane} \tag{4.1.3}$$

$$\mathbf{n} \times \mathbf{A} = 0 \qquad \text{in the vertical symmetry plane} \tag{4.1.4}$$

$$\mathbf{n} \times \mathbf{A} = 0 \qquad \text{at the outer surface of the yoke} \tag{4.1.5}$$

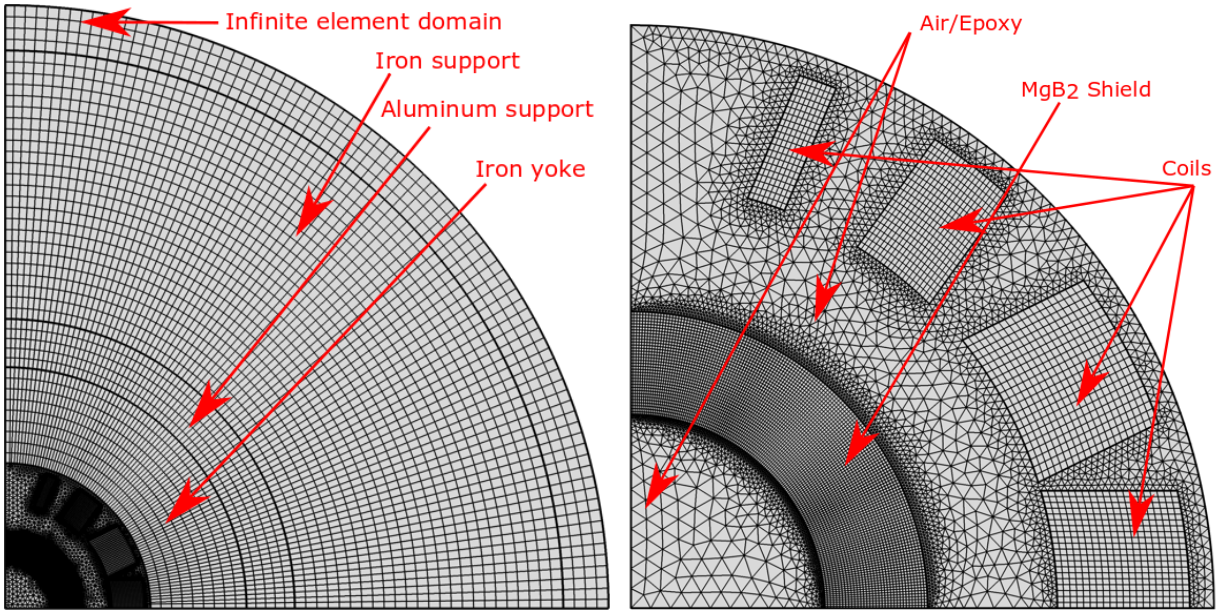

(a) Whole geometry and mesh

(b) Mesh around the shield and coils

Figure 4.1: Geometry and mesh of the MgB_2 model

The BC in the horizontal plane corresponds to a perfect magnetic conductor (i.e. no surface currents), while the other is a perfect magnetic insulation condition. The latter condition also ensures that the vector potential has no tangential components, thus the net current in these directions is zero. The parameters of the MCBY were taken from the magnet's technical drawings, available in the CERN technical drawing database (not public). The infinite element and the support domains were removed from the simulation since the iron yoke does not saturate at the

maximal current, so the solution in these domains would be negligible. The maximal element size in the shield and the iron yoke were 0.25 mm and 3.75 mm. Wherever it was possible, a mapped mesh was used, since the condition number of the stiffness matrix is better if the skewness and size of the mesh elements are homogeneous. The solution is closer to the true critical state if the value of A_r in Eq. 4.1.2 is small. Unfortunately, the simulation gets unstable as the value decreases. $A_r = 30\ \frac{\mu Wb}{m}$ was found sufficiently small to get accurate results and keep the simulation stable. Even with this value, the ramp of this parameter was necessary. Simulations have been run with larger values of A_r, and the results were used as initial condition for smaller values. This technique is called "non-linearity ramp", and is often used in highly non-linear problems. The effect of the value of the A_r parameter on the sharpness of the transition is demonstrated in Fig. 4.2.

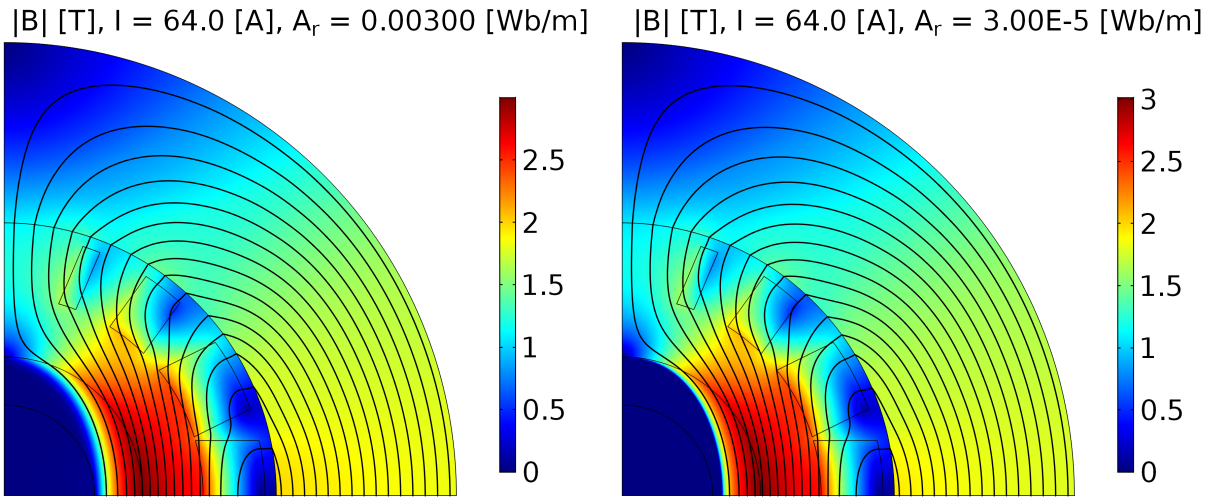

(a) Large value of A_r

(b) Small value of A_r

Figure 4.2: The effect of large and small A_r on the magnetic field

Figure 3.4 demonstrated the non-linear dependence of the external magnetic field on magnet current. This can be used to estimate the parameters of the $J_c(B)$ curve. The effect was simulated using Campbell's method, with several different values of the critical current density parameters J_0 and γ [22]. For each parameter value the deviation between simulation and experiment was calculated as

$$\chi^2 = \sum_i \left[B_{sim}(I_i) - B_{exp}(I_i)\right]^2 \tag{4.1.6}$$

where I_i=10,20,30,40,50 and 60 A. Figure 4.3 shows the values of χ^2 as a function of the parameters J_0 and γ. There is no clear minimum, several different values can closely reproduce the measured effect (see Fig. 4.3 (b)). In the following analyses J_0=7.5·10$^9\,\frac{A}{m^2}$ and γ=1.4 were used as starting values in the time-dependent simulations.

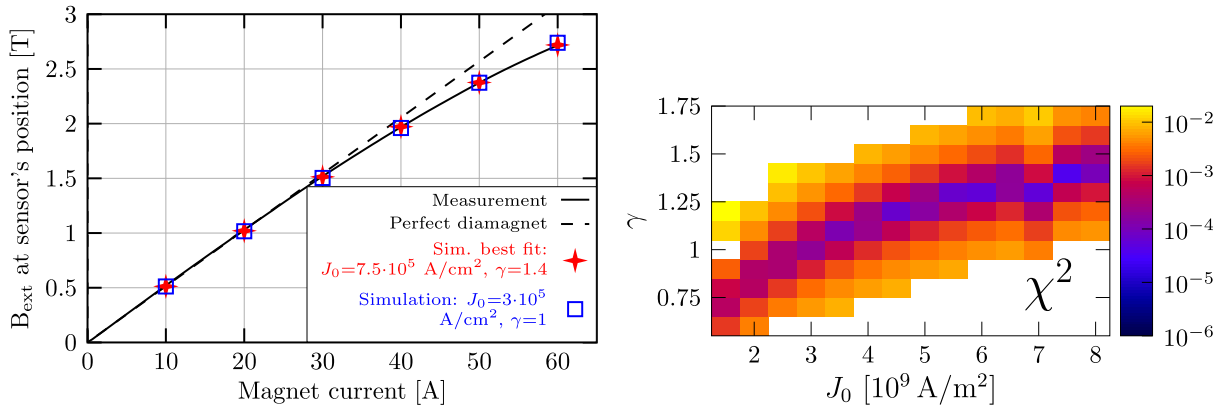

(a) Nonlinear increase of the magnetic field

(b) χ^2 for J_0 and γ values

Figure 4.3: The effect of large and small A_r on the magnetic field

The insulation boundary condition was modified to

$$\mathbf{n} \times \mathbf{E} = 0 \tag{4.1.7}$$

since in this formulation, no vector potential is used. A nonlinear magnetic material was used for the yoke, with the experimentally measured H-B curve as the constitutive relation. To consider the laminated construction of the iron yoke, its conductivity was reduced to $\sigma = 10^{-2}$ $\frac{S}{m}$ to suppress the induced currents during the time-dependent simulation. The magnet winding is constructed from standard twisted multifilament superconducting cables, which ensures a homogeneous distribution of the currents across their cross section. Therefore the same trick (i.e. a low conductivity) was applied to the material of the winding to suppress the eddy currents, which would have led to an uneven current distribution. The magnet current was implemented as an *External Current Density* node in COMSOL.

As the E-J characteristics, the regular power law was used, since the current density in our application should not pass the maximal J_c of the material.

$$E = E_0 \left(\frac{J}{J_c(B)} \right)^n = E_0 \left(\frac{J}{J_0 e^{-\gamma B}} \right)^n \tag{4.1.8}$$

The typical value of n is between 50 and 100. It basically controls the rate of relaxation in time, since the persistent currents feel larger 'resistance' (because for large n the power-law is much more 'rectified') for the same J value (below J_c) at lower ns, thus they decay faster. In this case, $n = 100$ was used. If the current ramps take much smaller time than the characteristic rate of relaxation, the effect of relaxation can be neglected, and for large n values, the results can be compared to Campbell's model results. The E_0 parameter was chosen to be $100\frac{\mu V}{m}$ [25].

Since these time-dependent simulations are highly non-linear, they ran really slow. To speed up the simulation, the mesh density was reduced by a factor of 4 compared to the mesh of Campbell's model, but the 'composition' of the mesh (i.e. the ratio of triangular and rectangular

elements) was kept the same. This way some overshoots were present inside the shield. With the upper mentioned parameters, the first 1700 seconds of the experimental current cycle was used as the current of the coils in the simulation. It has run in 26 hours on a desktop workstation with an Intel i7 5820K 3.3 GHz hexacore CPU and 32 GBs of RAM.

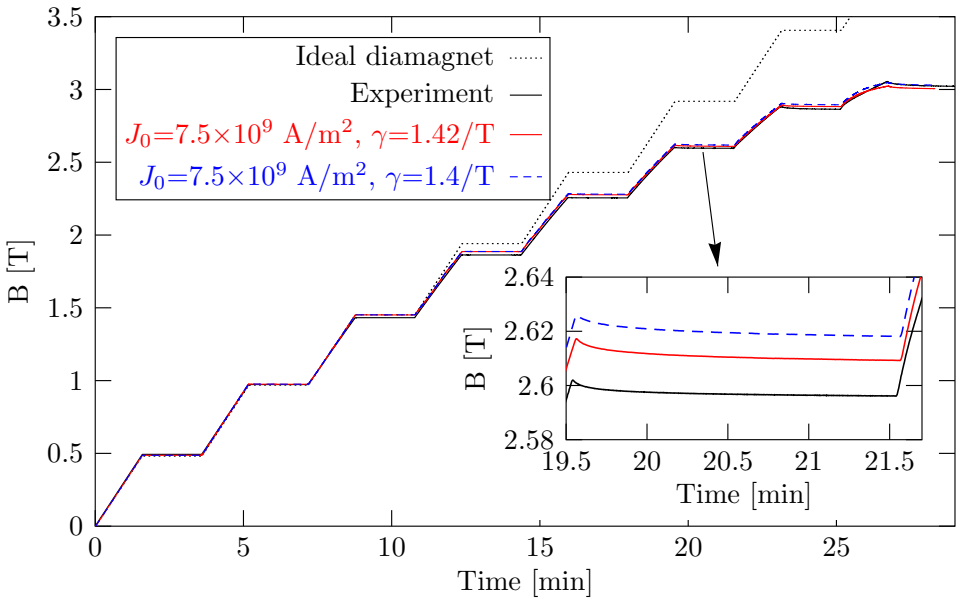

Figure 4.4: Numerical results on MgB_2 compared to the experiment

Figure 4.4 shows the results of the simulation. The blue curve shows the results got with the best parameters from Campbell's model. An increase to $\gamma = 1.42$ slightly improved the results. Probably better results could have been gotten with even larger values of γ, and/or smaller values of n. Due to the duration of the simulation, a proper parameter estimation was out of the scope of this work, but the numerical results are in really good agreement with the experimental ones despite the multiple simple parameter estimations. This simulation is also a proof of 'concept' that Campbell's model can be used for quick estimation of the parameters of the critical current density which later can be used in more accurate models.

4.2. Numerical explanations of the NbTi/Nb/Cu experimental results

4.2.1. Field penetration through the gaps

The simulations, in this case, are based on the same two models used in the case of MgB_2, but a few modifications of the model in COMSOL were necessary. The shield was modelled as 4+4 independent semi-circular layers of superconductor, with a gap of 0.5 mm between the upper and lower halves. All shield layers were then rotated by 1.5° around their common centre. These parameters seemed to roughly agree with those of the experimental setup. Because of this rotated cut, the system has no mirror symmetry anymore in the horizontal and vertical planes,

the whole geometry had to be modelled. Similarly to the MgB_2 case, the yoke was not saturated at the maximal applied magnetic field, thus the support parts were removed from the simulation. The mesh was constructed based on the same principles as in the other case; mapped mesh in the shield, yoke and coils, triangular mesh in the irregular zones. The geometry and the mesh near the cut on the right side of the shield are shown in Fig. 4.5.

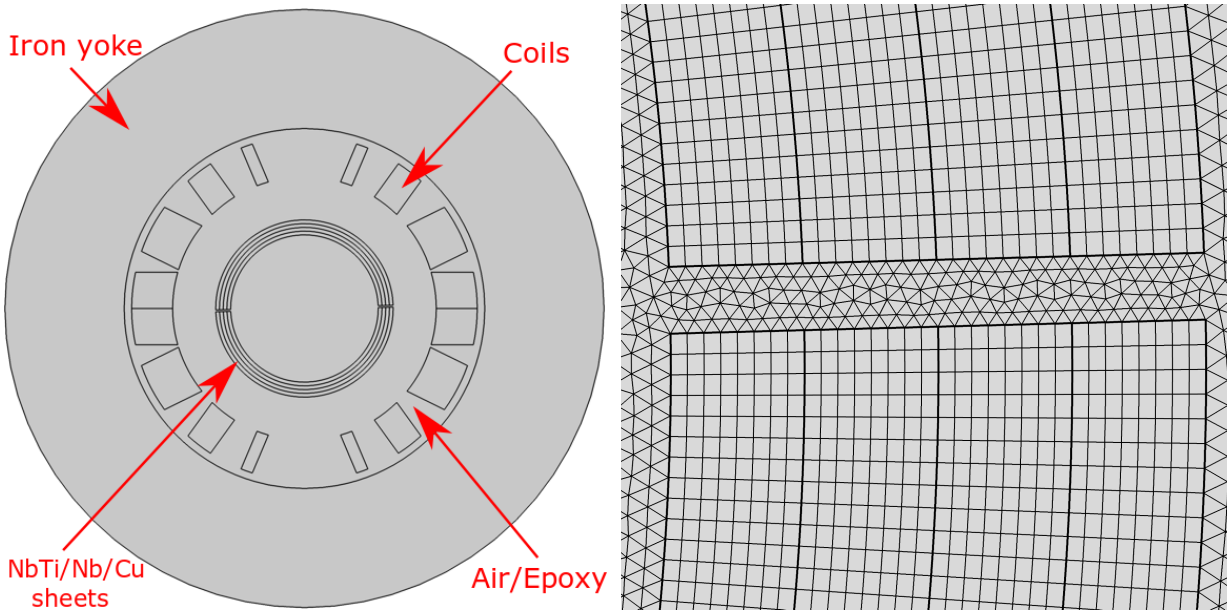

(a) The whole geometry (b) Mesh around the shield

Figure 4.5: Geometry and mesh of the NbTi model

Since the system has no mirror symmetry anymore, the original model had to be extended. In the original equation (Eq. 2.2.5) the sign of the persistent currents changes at $A_z = 0$. Mirror symmetry ensures that $A_z = 0$ in the interior of the shield, and the shielding currents on the two sides of the shield are induced symmetrically, with opposite signs. This results in a zero net current in the shield, in agreement with the fact that the shield is a floating object with no current leads, i.e. no net current through its cross section. With the broken symmetry of the current setup extra measures are needed to enforce this condition. The expression of the persistent currents, Eq. 4.1.2 was extended to

$$J_{Cb}^{(i)} = -J_c(B) \tanh\left(\frac{A_z - A^{(i)}}{A_r}\right) \tag{4.2.1}$$

where i=1..8 indexes the individual half-cylindrical shield components, and $A^{(i)}$ is the value of the vector potential in the non-magnetized region of that sheet. The parameters $A^{(i)}$ are not known a-priori, and are therefore further degrees of freedom of the problem. Their value can be calculated using the constraint of zero net current, implemented via the 'Global Equations' node

of COMSOL:

$$\int_{S^{(i)}} J_{Cb}^{(i)} \, \mathrm{d}^2 r = 0 \tag{4.2.2}$$

where $S^{(i)}$ is the cross section of the sheet i. This is analogous to the fixing the zero-potential level in electrostatics. The $J_c(B)$ curve was taken from experimental data from [24] (Figure 2, Parallel 350 °C heat treatment), so the optimization of J_0 and γ parameters was not necessary. The calculated magnetic field in this geometry is shown in Fig.4.6 for a magnet current 55 A.

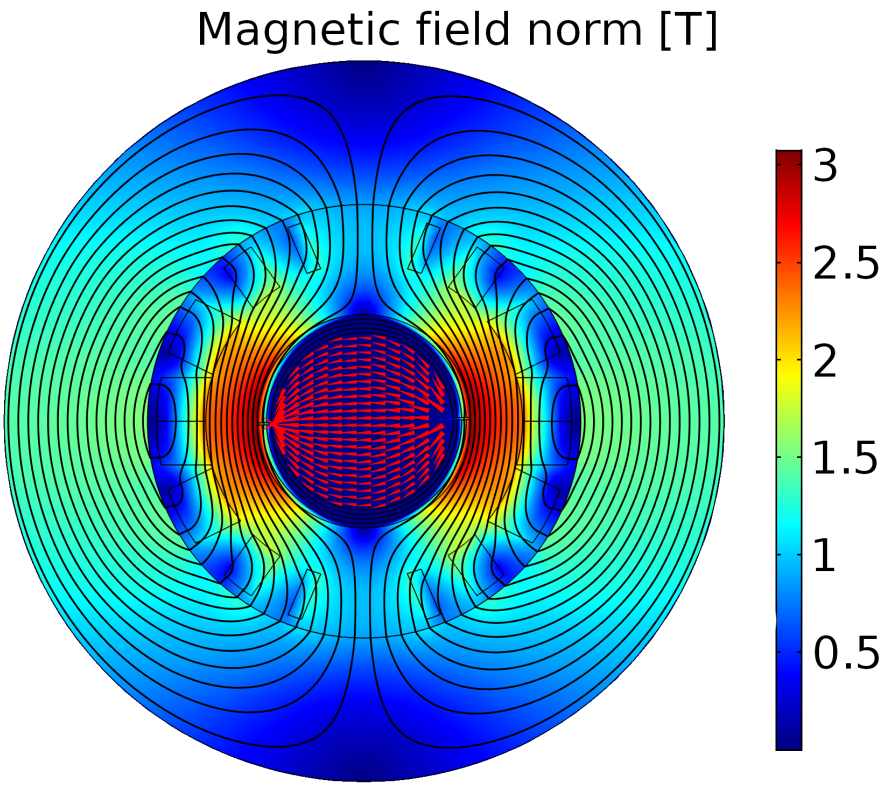

Figure 4.6: Magnetic field in the NbTi/Nb/Cu multilayer geometry.

Inside the shield, the arrow plot is on a logarithmic scale. The arrow plot indeed shows that there is a horizontal magnetic field inside the shield, with almost zero vertical component in the middle. This is in great agreement with the experimental results discussed in the previous section. Figure 4.7 shows the values of B_x (vertical) and B_y (horizontal) components of magnetic field inside the shield in the horizontal midplane. The figure shows that the magnetic field at the origin is ≈ 15 mT in the horizontal direction and ≈ 0.4 mT in the vertical direction. This has the same order of magnitude in both cases as shown in Fig. 3.10. This implies that the numerical model is able to describe our experiments. With the same rotation of the shield but with one cut removed, like in Fig. 3.6c, the field inside drops to 10^{-8} mT which is two orders of magnitude smaller, than the relative tolerance value of the simulation. This supports the statement that

the penetration of the field into the shield is caused by the cuts, and not by the unsatisfactory behaviour of the material.

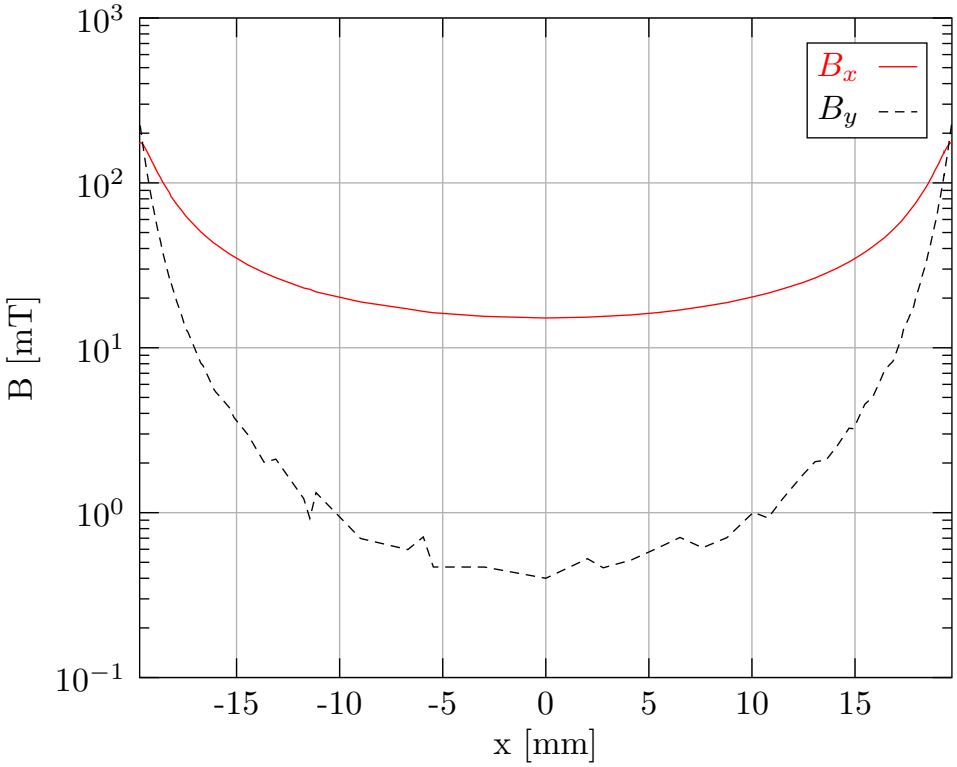

Figure 4.7: Horizontal magnetic field profile inside the shield

As previously mentioned, for the same geometry, but with an ideal diamagnet instead of a real superconductor, the inner sensors should measure a field which is increasing linearly with magnet current.

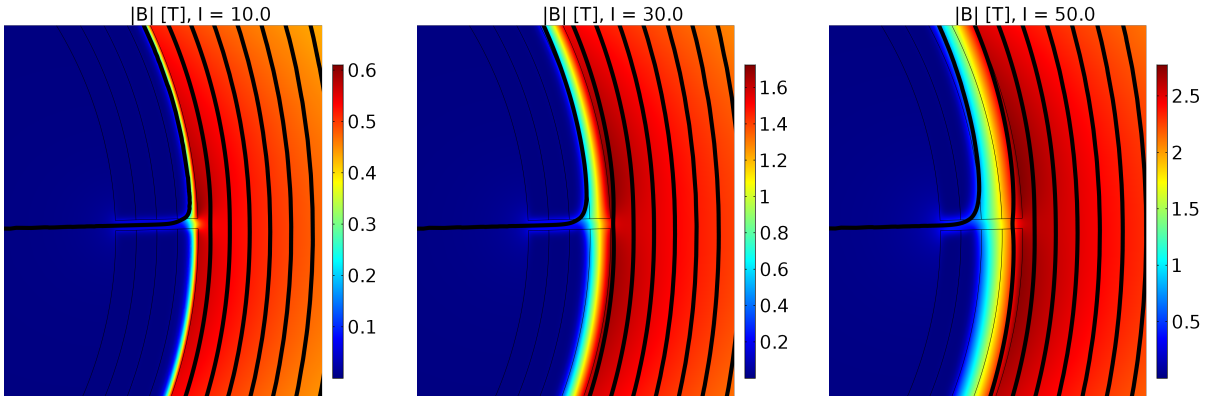

(a) 10 A coil current (b) 30 A coil current (c) 50 A coil current

Figure 4.8: The virtual widening of the gap due to penetrating magnetic field

Figure 4.8 shows the realistic case, where the magnetic field penetrates into the material,

which virtually widens the gap for larger external field. Since this penetration effect is non-linear with the external field, an additional, non-linear increase adds to the linear signal caused by the increasing external field by itself. This could explain the non-linear inner Hall-sensor signals shown in Fig. 3.11.

4.2.2. Demagnetization

To understand what exactly happens during demagnetization inside the material, an eddy current simulation was run with the same current cycle as that used in the experiment, except that the ramp rate of the coil current was significantly faster (10.8 $\frac{A}{s}$), and the plateaus were removed in order to get the results quicker. The cuts were removed to restore the symmetry of the system and be able to simulate only one-quarter of the geometry. Furthermore, the shield was modelled as one thicker layer, instead of four different.

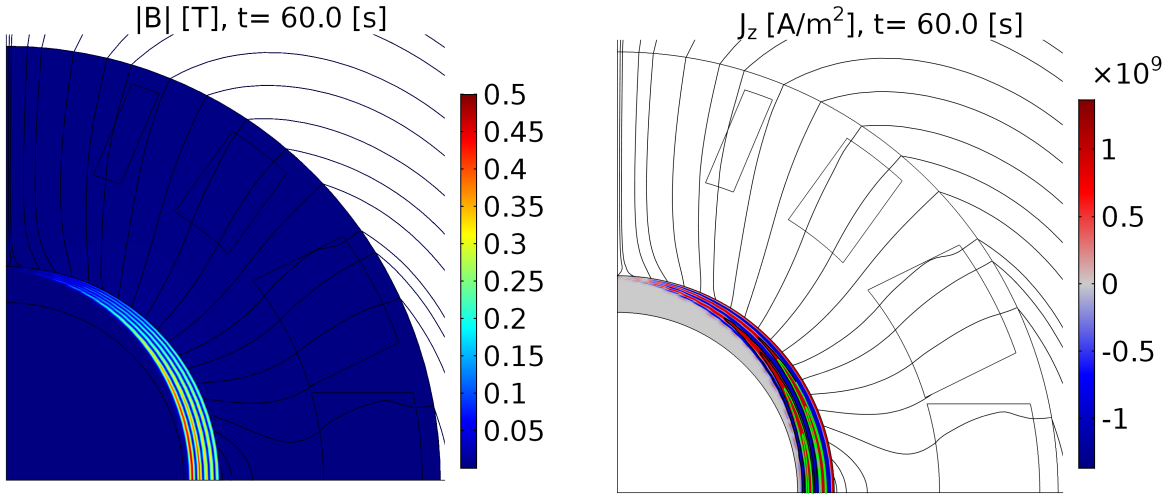

(a) Field pattern of the trapped magnetic field

(b) Pattern of the persistent currents

Figure 4.9: Magnetic field and persistent current pattern at the end of the demagnetization cycle

Figure 4.9a and Fig. 4.9b show the pattern of the magnetic field and the persistent currents, after the complete demagnetization cycle. Figure 4.9a shows that layers of the trapped magnetic field are inside the shield. First J_c flows in the negative z direction (positive coil current), at the depth corresponding to this current. As the maximal current is reached, the current is ramped down to a negative current value, the absolute value of which is smaller than the previous maximum. This 'stacks' a current layer flowing in the positive z direction and since the current is smaller, the penetration depth of the magnetic field is smaller than in the previous ramp. At this point, there are two current 'layers' flowing with J_c in the $\pm z$ directions separately, forming a dipole-like structure. Repeating the same up-down ramp with decreasing magnitude in each

step, multiple current layers are 'stacked' in the material. This way the induction lines of the dipole structures can close inside the material. The schematic representation of this process is shown in Fig. 4.10. Even though this is not a true virgin-state, since the microscopic field-pattern of the shield carries the history of it, the stray field at the Hall sensors is sufficiently small for our applications.

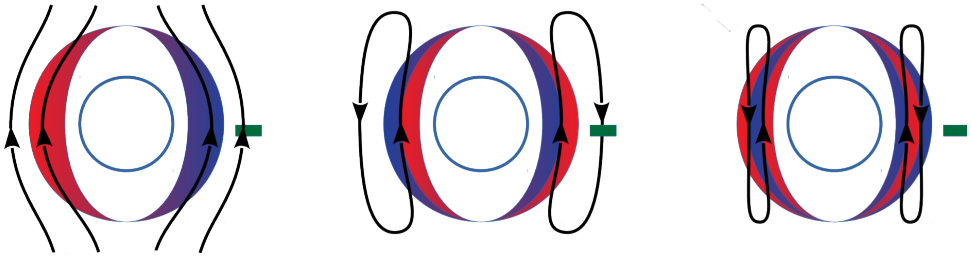

Figure 4.10: The schematic structure of dipoles forming inside the material

The similarity between the numerical and experimental results is remarkable. The differences can be explained with the more than 100 times faster ramp rate, and the removed plateaus. This way the relaxation has significantly smaller effect in the simulations than in the measurement. The differences between the used $J_c(B)$ and the actual $J_c(B)$ of the material used could also have influence on the results.

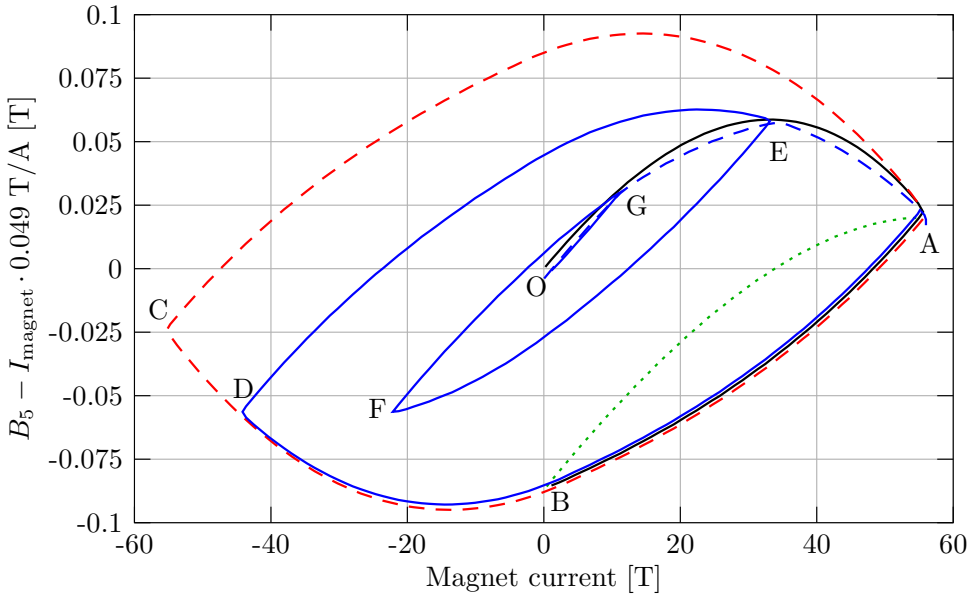

Figure 4.11: Demagnetization simulation of NbTi/Nb/Cu multilayer

5. Conclusion and Further Plans

During my work I have gained an incredible amount of experience both in magnetic experiments, and finite element simulations. I have also acquired a lot of knowledge about the working principle of the modern particle accelerators. The measurements were all performed in CERN's SM18 facility, so I have experienced what it is like working in an international team. Two different materials were tested, and both of them performed very well during the tests. Both of them would be a good candidate material for the construction of the complete SuShi septum magnet.

5.1. Design of the CCT SuShi

In this subsection, I will present some of the preliminary design results of our proposed CCT-like septum magnet. The CCT acronym stays for 'Canted-Cosine-Theta', which is a magnet design proposed in the '70s, but not really used so far because it uses significantly more superconducting cable than the regular design. It consists of two separate windings which are tilted with $+\alpha$ and $-\alpha$ degree and placed on the surface of a cylinder. The currents in the two windings are flowing in the opposite direction. This way the longitudinal component of the two windings cancel, while the transversal components add up, creating a homogeneous field. The advantage of this kind of magnet compared to a regular one is its exceptional mechanical stability. The place for the coil windings can be cut into aluminium cylinders with CNC machines. After epoxy impregnation, this would result in an extremely stable mechanical structure, which could significantly reduce the length of the necessary quench training of the magnet. Furthermore, the production of a CCT-like magnet is low-tech, does not need expensive infrastructure. Figure 5.1 shows our proposed design. A 2D Campbell simulation has been run with MgB_2 as a material, to ensure that the penetration of magnetic field does not cause any problem in the field homogeneity.

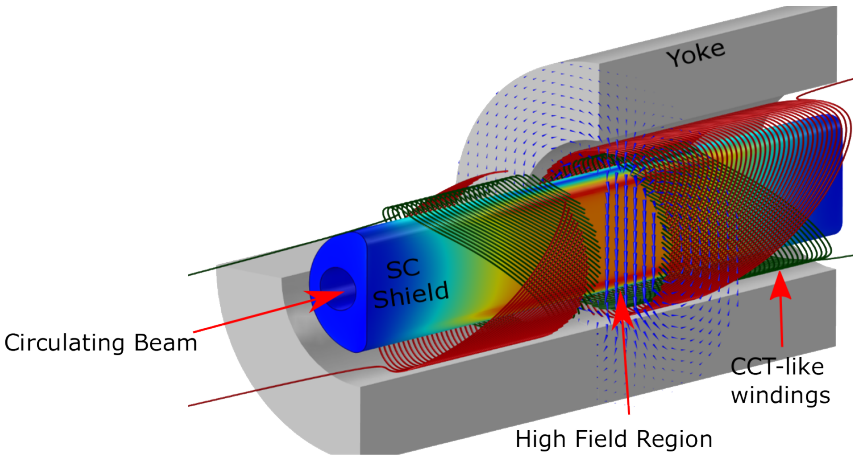

Figure 5.1: The schematic presentation of the CCT SuShi septum

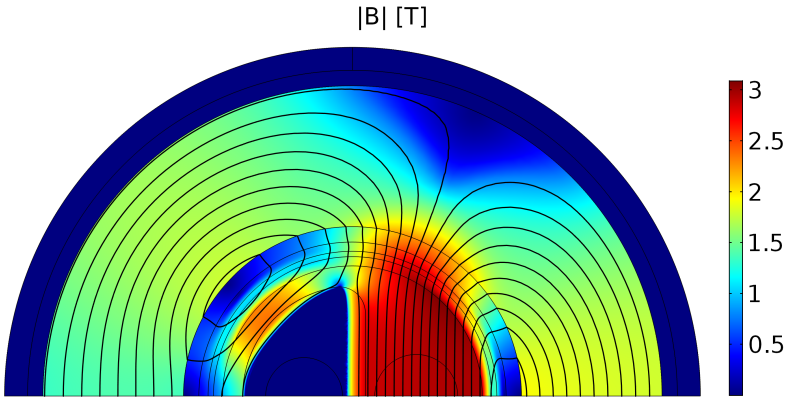

Figure 5.2: 2D Campbell simulation of the proposed design of CCT SuShi

The current density inside the coils were determined with multipole expansion, and the amplitude of the harmonic components has been determined with SVD. The proposed design of the complete magnet is shown in Fig. 5.3.

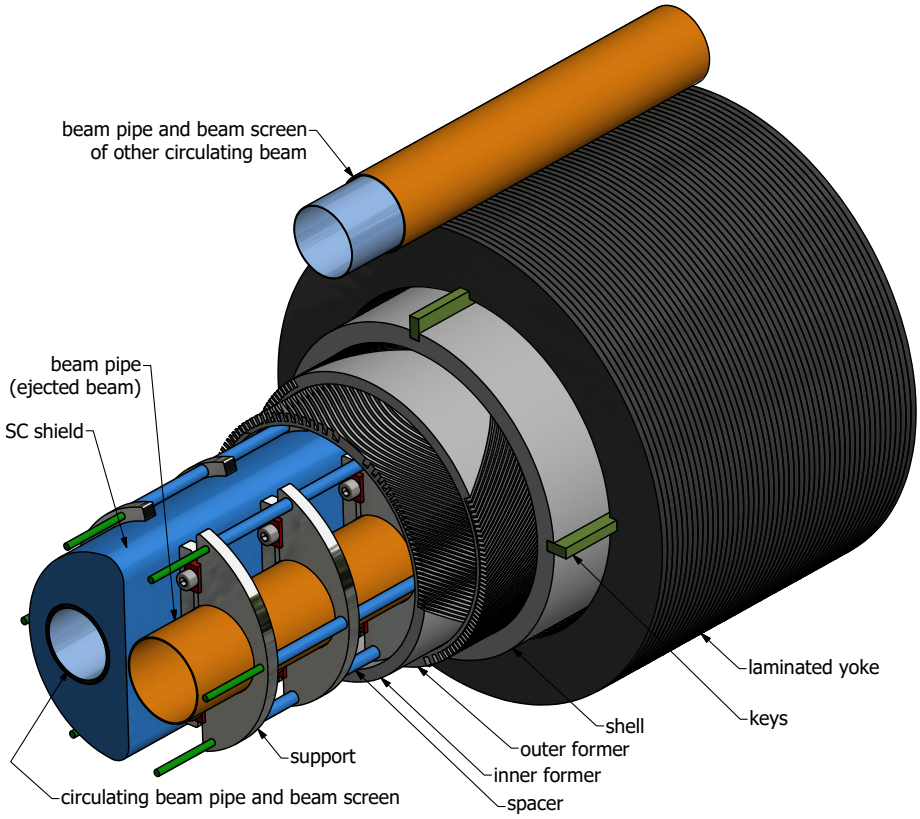

Figure 5.3: Technical drawing of the proposed CCT SuShi

To mount the shield into the magnet, multiple aluminium elements would be placed into the bore, noted with green in the technical drawing (Fig. 5.4). The beam pipe of the extracted

beam would be placed into half-moon shaped aluminium support elements which would be strung onto a spacer rod. C-shaped aluminium support elements would hold the shield itself in position. Rectangular elements would be placed between the shield's flat surface and the half-moon shaped support elements, and special screws would be placed between them, which would push the rectangular element to the shield's surface, and the support element to the wall of the inner aluminium former when stretched. This way the shield and the beam pipes could be kept in place.

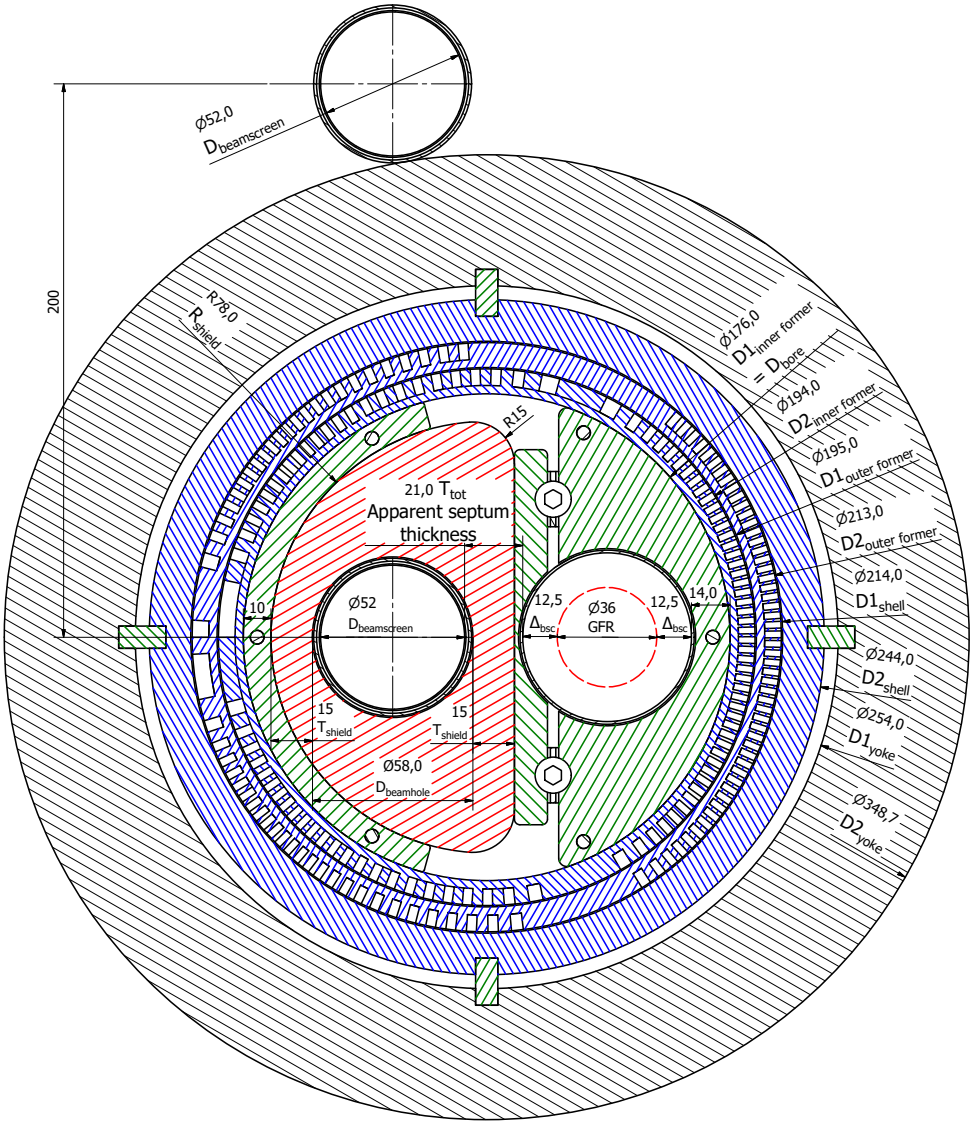

Figure 5.4: Technical drawing of the proposed CCT SuShi

Even though the geometrical design of the magnet seems finished, there are lots of other challenges in this project. Despite that both materials performed well in the experiments, both

have disadvantages. For MgB_2, the manufacturing of special shapes, and longer tubes needs R&D, for NbTi/Nb/Cu multilayer, the only barrier is its very high current price since Nippon Steel stopped the production of it. Negotiations with Mr Itoh, the inventor of this material have been started about transferring the production technology either to CERN or to Hungary. Hopefully, this would reduce the price of the material. Furthermore, a complete quench protection system of the magnet has to be designed which states numerical challenges, because it is a heavily coupled multiphysics simulation. In the future, I am planning to pursue a PhD with the complete design, production and the testing of the magnet. This would include further numerical studies, like the mechanical modelling, and the design of the quench protection system. Until the middle of 2020 with the group I am working with, we would like to build a real prototype of the magnet, and test it in 2021.

6. Acknowledgemens

In this way, I would like to thank my supervisor Dániel Barna both for his professional and stylistic comments and corrections of my thesis, which greatly improved the quality of my work, and my ability of scientific writing. I hope that some of his work morale and precision stuck on me during our common work.

I would also like to thank my classmate Kristóf Brunner and the staff of the SM18 facility, especially to Carlo Petrone, Max Pascal and Jerome Feuvrier for their great help in the measurements of NbTi/Nb/Cu multilayer.

I would like to thank my family; To my parents for their support and hard work which made possible for me to concentrate on studying with my whole capacity without any necessity, and to my partner Korinna for her encouragement and her patience in my stressful periods.

At last but not at least I would like to thank my high-school physics teacher Éva Kiss who made me love this science. Without her work probably I would not even apply to higher education.

The SuShi Septum project has received funding from the FCC Study Group, the European Unions Horizon 2020 research and innovation programme under grant agreement No 730871 (ARIES), and from the Hungarian National Research, Development and Innovation Office under grant #K124945.

References

[1] Andrew Robert Steere. A Timeline of Major Particle Accelerators, MSc Thesis, Michigan State University (2005)

[2] J.D. Cockcroft and E.T.S. Walton. Experiments with high-velocity ions, Proc. Royal Soc., Series A 136 (1932), 619–30.

[3] CERN website about the accelerator complex

[4] CERN website about the ATLAS experiment

[5] AC Team, Diagram of an LHC dipole magnet, CERN-DI-9906025, (1999)

[6] LHC Design Report Volume 1, Chapter 17

[7] LHC Design Report Volume 1, Chapter 8

[8] Godeke, A., Cheng, D., Dietderich, D.R., Ferracin, P., Prestemon,S.O., Sa bbi, G., and Scanlan, R.M.: Limits of NbTi and Nb3Sn, and Development of W&R Bi-2212 High Field Accelerator Magnets. United States: N. p., 2006. Web.

[9] A. Lechner, W. Bartmann, F. Burkart, M. Calviani, M.I. Frankl, S. Gilardoni, B. Goddard, T. Kramer, A. Perillo Marcone, E. Renner: Dilution Requirements for the FCC-hh beam Dump, FCC Week Amsterdam 4AMS09C talk, (2018)

[10] G. Borghello: An Unprecedented Challenge for MOS Transistors, FCC Week Amsterdam 4AMS10C talk, (2018)

[11] Bean, C. P. (1962): Magnetization of hard superconductors. Physical Review Letters, 8(6), 250–253. https://doi.org/10.1103/PhysRevLett.8.250

[12] Bean, C. P. (1964): Magnetization of high-field superconductors. Reviews of Modern Physics, 36(1), 31–39. https://doi.org/10.1103/RevModPhys.36.31

[13] Campbell, A. (1971): The interaction distance between flux lines and pinning centres. Journal of Physics C: Solid State Physics, 4(18), 3186–3198. https://doi.org/10.1088/0022-3719/4/18/023

[14] Campbell, A. (2007): A new method of determining the critical state in superconductors. Superconductor Science and Technology, 20, 292–295. https://doi.org/10.1088/0953-2048/20/3/031

[15] Wolsky, A. M., & Campbell, A. M. (2008). A new method for determining the critical state of three-dimensional superconductors: explanation and examples. Superconductor Science and Technology, 21(7), 075021. https://doi.org/10.1088/0953-2048/21/7/075021

[16] Anderson, P. W., Kim, Y. B. (1964): Hard superconductivity: Theory of the motion of Abrikosov flux lines. Reviews of Modern Physics, 36(1), 39–43. https://doi.org/10.1103/RevModPhys.36.39

[17] Yeshurun, Y., Malozemoff, A. P. (1996): Magnetic relaxation in high-temperature superconductors, 68(3), 911–949. https://doi.org/10.1103/RevModPhys.68.911

[18] Duron, J., Grilli, F., Dutoit, B., Stavrev, S. (2004): Modelling the E-J relation of high-Tc superconductors in an arbitrary current range. Physica C: Superconductivity and Its Applications, 401(1–4), 231–235. https://doi.org/10.1016/j.physc.2003.09.044

[19] Giunchi, G. (2003): High density MgB_2 obtained by reactive liquid Mg infiltration. International Journal of Modern Physics B, 17(04n06), 453–460. https://doi.org/10.1142/S0217979203016091

[20] Giunchi, G. Turrioni, D. Kashikhin, V. Hogan, N. and Barzi, E.: Feasibility Study of a MgB_2 Superconducting Magnetic Cloak, IEEE Transactions on Applied Superconductivity, Vol. 26, NO. 3, April 2016

[21] Giunchi, G. Saglietti, L. Ripamonti, G. Figini A.A. Bassani, E. and Perini, E.: Superconducting Joints Between MgB_2 Wires and Bulks, IEEE Transactions on Applied Superconductivity, Vol. 20, NO. 3, June 2010, pp 1524

[22] Barna, D: First experimental results with a superconducting shield (SuShi) septum prototype, FCC Week Berlin 4TH09B talk (2017)

[23] Itoh, I., Sasaki, T. (1993): Magnetic Shielding Properties of NbTi/Nb/Cu Multilayer Composite Tubes. IEEE Transactions on Applied Superconductivity, 3(1), 177–180.

[24] Itoh, I., Sasaki, T. (1995): Critical Current Density of superconducting NbTi/Nb/Cu Multilayer Composite Sheets. Cryogenics, 35(6), 403–404.

[25] Stephan Russenschuck: Field Computation for Accelerator Magnets: Analytical and Numerical Methods for Electromagnetic Design and Optimization

STATEMENT

Name: Novák Martin István
NEPTUN code: YUCD6U
ELTE Faculty of Science: Physicist MSc
Title of thesis: Numerical and experimental study of superconducting magnetic shields for the construction of a high field septum magnet

As the author of this thesis I declare that it is my own work and that I have acknowledged and referenced the work and ideas of others.

Budapest, 2018.05.31.

.....
Signature